POLITECNICO DI TORINO
Repository ISTITUZIONALE

Code-Based Differential GNSS Ranging for Lunar Orbiters: Theoretical Review and Application to the NaviMoon Observables

Original
Code-Based Differential GNSS Ranging for Lunar Orbiters: Theoretical Review and Application to the NaviMoon Observables / Delepaut, A.A.A., Minetto, A., Dovis, F.. - In: REMOTE SENSING. - ISSN 2072-4292. - ELETTRONICO. - 16:15(2024). [10.3390/rs16152755]

Availability:
This version is available at: 11583/2991287 since: 2024-07-30T10:29:34Z

Publisher:
MDPI

Published
DOI:10.3390/rs16152755

Terms of use:

This article is made available under terms and conditions as specified in the corresponding bibliographic description in the repository

Publisher copyright

(Article begins on next page)

09 November 2026

remote sensing

MDPI

Article

Code-Based Differential GNSS Ranging for Lunar Orbiters: Theoretical Review and Application to the NaviMoon Observables

Anaïs Delépaut *, Alex Minetto and Fabio Dovis

Department of Electronics and Telecommunications (DET), Politecnico di Torino, 10129 Torino, Italy; alex.minetto@polito.it (A.M.); fabio.dovis@polito.it (F.D.)
* Correspondence: anais.delepaut@polito.it

Abstract: In the near future, international space agencies have planned to achieve significant milestones in investigating the utilization of Global Navigation Satellite Systems (GNSS) within and beyond the current space service volume up to their application to lunar missions. These initiatives aim to demonstrate the feasibility of GNSS navigation at lunar altitudes. Based on the outcomes of such demonstrations, dozens of lunar missions will likely be equipped with a GNSS receiver to support autonomous navigation in the lunar proximity. Relying on non-invasive, consolidated differential techniques, GNSS will enable baseline estimation, thus supporting a number of potential applications to lunar orbiters such as collaborative navigation, formation flight, orbital manoeuvers, remote sensing, augmentation systems and beyond. Unfortunately, the large dynamics and the geometry of such differential GNSS scenarios set them apart from current terrestrial and low-earth orbit use cases. These characteristics result in an increased sensitivity to measurements time misalignment among orbiters. Hence, this paper offers a review of baseline estimation methods and characterizes the divergences and limitations w.r.t. to terrestrial applications. The study showcases the estimation of the baseline length between a lunar CubeSat mission, VMMO, and the communication relay Lunar Pathfinder mission. Notably, real GNSS measurements generated by an Engineering Model of the NaviMoon receiver in the European Space Agency (ESA/ESTEC) Radio Navigation Laboratory are utilized. A radio-frequency constellation simulator is used to generate the GNSS signals in these hardware-in-the-loop tests. The performed analyses showed the invalidity of common terrestrial differential GNSS ranging techniques for space scenarios due to the introduction of significant biases. Improved ranging algorithms were proposed and their potential to cancel ranging errors common to both receivers involved was confirmed.

Keywords: differential GNSS; baseline estimation; inter-spacecraft range; lunar orbiters; GNSS in space

check for updates

Citation: Delépaut, A.; Minetto, A.; Dovis, F. Code-Based Differential GNSS Ranging for Lunar Orbiters: Theoretical Review and Application to the NaviMoon Observables. *Remote Sens.* **2024**, *16*, 2755. https://doi.org/10.3390/rs16152755

Academic Editor: José Darrozes

Received: 31 May 2024
Revised: 15 July 2024
Accepted: 24 July 2024
Published: 28 July 2024

Copyright: © 2024 by the authors. Licensee MDPI, Basel, Switzerland. This article is an open access article distributed under the terms and conditions of the Creative Commons Attribution (CC BY) license (https://creativecommons.org/licenses/by/4.0/).

1. Introduction

Given the momentum taken by the space sector for lunar exploration both by private and governmental actors, scientific and commercial initiatives are expected to expand in the 2020s, led by the European Space Agency (ESA)'s Moonlight initiative and National Aeronautics and Space Administration (NASA)'s Artemis program [1]. In this framework, the development of guidance, navigation, and control solutions being independent of tracking and controlling ground segments is strongly desired for lunar exploration. In particular, the south pole region of the Moon is attracting attention from the perspective of human activity bases and exploration [2–5]. In this context, the ESA and NASA together with the Italian Space Agency (ASI) plan to fly in-orbit demonstration missions around the Moon. These missions are the Surrey Satellite Technology Ltd (SSTL) Lunar Pathfinder which is planned to be flying the NaviMoon receiver in 2025, [6], and the Firefly Blue Ghost Mission 1 flying a multi-constellation Global Navigation Satellite System (GNSS) receiver payload

in 2024 in the framework of the Lunar GNSS Receiver Experiment (LuGRE) [7]. Both will track Galileo E1, E5a, and GPS L1 C/A, L5 signals and will return pseudorange, carrier phase and Doppler measurements. The success of these two missions will then contribute to the extension of the Space Service Volume (SSV) to the cis-lunar space. SSV is defined as the volume in space currently spanning from 3000 km to 36,000 km above the Earth's surface, in which the availability and performance of GNSS signals are characterized [8].

In addition to being equipped with a navigation system and to being on or around the Moon at the same time [9], these missions will often be interacting as well, [10], potentially relaying communications for one another or act as distributed systems, given their effectiveness and cost efficiency when compared to monolithic missions [11]. The interactions between these various space objects around the Moon justify the need for developing inter-spacecraft ranging techniques applicable to the lunar vicinity. The family of Differential GNSS (DGNSS) ranging techniques have been used a lot in the past decades both on Earth and in space to improve the position of a specific user, given their non-invasiveness as they rely solely on a communication link among the interacting GNSS users.

1.1. DGNSS on Earth

In the field of terrestrial applications, differential GNSS techniques are used a lot through the creation of corrections for compensating atmospheric delays, satellite orbits and clock errors for both the GNSS pseudoranges in the field of DGNSS, [12–14], and of carrier phase in the field of Real Time Kinematic (RTK) for higher accuracy applications [14,15]. In both techniques, the corrections are inferred by using a fixed reference station with a well-known location and are transmitted to the user via radio, cellular networks, or the internet. When the baseline length between the user and the reference station becomes long, as is mostly the case for space scenarios, the literature for terrestrial applications based on differential GNSS measurements focus on the spatial decorrelation of the atmospheric delays with the increasing baseline [16–19]. Another type of collaborative positioning, known as DGNSS-Cooperative Positioning (CP), has been proven successful for terrestrial applications as well, such as in collaborative vehicle networks and mobile users [20,21]. This technique does not rely on a fixed reference station but, instead, works between two moving GNSS receivers [22,23]. The basic idea behind DGNSS-CP is to measure the relative distance between GNSS receivers by exchanging information about their respective pseudoranges to a common set of tracked GNSS satellites. More specifically, a user with poor GNSS visibility can share raw GNSS measurements through a communication link with another user to estimate their baseline vector. Subsequently, this relative distance can be used in the Position Velocity Time (PVT) solution estimation and improve the Dilution of Precision (DOP) of the positioning problem. Even when it is noisy and correlated to the other GNSS range measurements, this additional ranging information was proven to be beneficial in low visibility and high DOP scenarios [22].

1.2. DGNSS in Space

When it comes to ranging in space, the use of GNSS measurements has provided the primary method for determining the relative position of cooperating Earth orbiters in the last decades for applications such as formation flights, rendezvous and docking [24–27]. However, in such context, differential GNSS scenarios are more challenging given the larger dynamics of the end users and the larger distances involved in the process, leading to decorrelation of the atmospheric delays and satellite orbital errors between users [28–32]. Despite this obstacle, in 1997, ETS-7 was the first mission to use GNSS signals for relative navigation in space with meter-level accuracy [33]. In 2002, the Low-Earth Orbit (LEO) formation flight Gravity Recovery And Climate Experiment (GRACE) mission involving baselines up to 250 km achieved Precise Baseline Determination relying on GNSS measurements fused with Radio Frequency (RF) ranging. By processing carrier phase and pseudorange measurements after resolution of the double differences integer ambiguity, they achieved millimeter accuracy in post-processing using the Least Square Ambiguity Decorrelation Adjustment (LAMBDA)

method [34]. In 2014, the CanX-4/5 performed DGNSS-based baseline determination on cubesat avionics for the first time, reaching submeter-level accuracy [35]. However, integer ambiguity resolution has never been performed on board until now [36–38]. Limited onboard computational resources, imperfect knowledge of the spacecraft attitudes, and multipath may prevent the integer ambiguity resolution reducing the accuracy achievable in real-time. Estimation biases have been documented for legacy baseline estimation techniques in [39] where authors assessed a code-based differential ranging technique in LEO between cubesats with submeter-level accuracy. In [40], a kinematic technique based on differential pseudorange and carrier phase measurements is suggested for real-time precise baseline determination without Integer Ambiguity Resolution and applied in LEO.

1.3. DGNSS for the Moon

Transitioning to a lunar GNSS scenario, being the focus scenario of the present contribution, ionospheric delays become less of a concern as most of the GNSS signals received at lunar altitudes did not propagate through the ionosphere [41,42]. However, the relative dynamics between users orbiting the Moon become more complex as the typical stable lunar orbits are not circular as is the case for the terrestrial ones, given the presence of lunar mass concentrations [43]. Furthermore, the GNSS signals power levels received by a receiver in lunar orbit are weak causing the measurements to be noisier [41]. Hence, the measurements are affected by a large amount of uncorrelated errors and applying differential techniques could be less beneficial [42]. Also, in noisier environments and high dynamics systems, cycle slips are more frequent making the integer ambiguity resolution of the carrier phase measurements more challenging [44].

As a contingency scenario, the present contribution aims to assess the feasibility of GNSS-based differential ranging techniques between two lunar orbiters using only pseudorange observables. The importance and originality of this study lies in that it explores, for the first time, the applicability of DGNSS ranging to users in lunar orbits. Most significantly, the experimental analysis was performed on a real spaceborne receiver, namely the very first ESA GNSS receiver that will fly all the way to the Moon in the context of the ESA's Lunar Pathfinder mission. This research aims to contribute to a deeper understanding of the potential and limitations of DGNSS in space.

More specifically, this work shows that modeling assumptions used for linearization of the relationship between the inter-user vector and the pseudorange single and double differences taken for granted in terrestrial and LEO applications are violated in the case of lunar GNSS differential scenarios. Subsequently, it analyzes the possibility of updating the parallelism assumption while keeping the considered algorithm linear for low-complexity purposes and compares the common techniques with the updated ones. It shows that updating the modeling assumption significantly improved the performances with respect to the terrestrial standard algorithm by reducing the bias introduced by the increasing baseline. However, the performances seem to be bounded by the sum of the individual covariances on the measurements of each user involved in the process, as per the Absolute Positions Differencing (APD) presented in [23,45].

In practice, the results are obtained both theoretically through Monte Carlo simulations, by Matlab post-processing of data obtained from Systems Tool Kit (STK), and experimentally, in the Radio Navigation Laboratory of ESA, making use of GNSS observables generated by a GNSS receiver specifically designed for a Moon mission, through a Hardware-in-the-Loop (HWiL) set-up. The Moon receiver is called the NaviMoon and will be hosted by the Lunar Pathfinder space mission [46].

The paper is structured as follows: Section 2 describes the fundamentals of the GNSS-based baseline estimation, describes the limitations of this assumption for a space scenario and proposes potential updates in the algorithm. Section 3 describes the space scenario considered for the present analysis, the architecture of the theoretical Monte Carlo simulations as well as the functional blocks of the test bench designed to test the presented techniques on the NaviMoon receiver. Finally, Section 4 presents the results achieved with

this environment and Section 5 discusses the potential performances of inter-spacecraft GNSS ranging in space, showing that the various techniques presented seem to be lower bounded by taking the difference of the individual Single Point Position (SPP).

2. Background

2.1. Code-Based GNSS Inter-User Ranging Techniques

By considering a pair of moving users (i.e., spacecraft) i and j, at a given time instant k, relative ranging technologies allow to estimate their *inter-user range* (a.k.a. *baseline length*)

$$d_{ij,k} = ||\mathbf{d}_{ij,k}|| = ||\mathbf{x}_{j,k} - \mathbf{x}_{i,k}|| \tag{1}$$

where the operator $||\cdot||$ is the Euclidean norm and $\mathbf{x}_{i,k}$, $\mathbf{x}_{j,k}$ are the actual locations of the users in a given Cartesian reference frame. While radio-frequency ranging solutions directly provide an estimate of Equation (1) by means of signal Time of Flight (ToF) or Round-trip Time (RTT), DGNSS techniques first estimate a displacement vector, a.k.a. *baseline vector*

$$\mathbf{d}_{ij,k} = \begin{bmatrix} \Delta x_{ij,k} & \Delta y_{ij,k} & \Delta z_{ij,k} \end{bmatrix}. \tag{2}$$

Through DGNSS techniques, the inter-user range estimation can be obtained by applying the Euclidean norm to an estimate of Equation (2), namely $\hat{\mathbf{d}}_{ij,k}$.

The DGNSS estimation of the inter-user range can be achieved through a few differential methods [23], based on the combination of pseudorange measurements from independent, networked GNSS receivers, following the exchange of these data from one user, defined as the *aiding user*, to another, the *aided user*, as depicted in Figure 1a. Different algorithms can be selected according to their capability of canceling the systematic biases at stake (i.e., receiver and satellite clock biases and satellites orbit biases) [47], at the cost of an increased output variance [48]. Despite the fact that ionospheric and tropospheric errors can be reasonably neglected at lunar distances, other common sources of error may affect the spaceborne receivers and could be effectively compensated through these techniques.

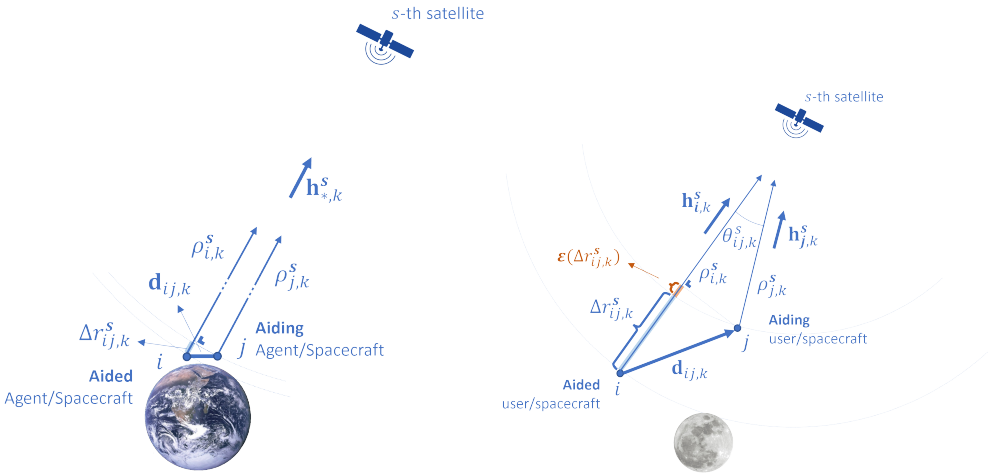

(**a**) Parallelism assumption valid. (**b**) Parallelism assumption invalid.

Figure 1. Pictorial view of differential GNSS ranging both for terrestrial applications and space scenarios. The symbol * denotes the user id where it can be either i or j.

Given the high dynamics inherent in a differential GNSS scenario involving lunar orbiters, the effect of the time offset between the GNSS observables of the two receivers is amplified, meaning that the baseline will have changed significantly over this time offset. Therefore, in all the techniques presented here below, the pseudoranges of the *aiding user* are considered to be shared to the *aided user* such that they can subsequently be subject to a

time-compensation to be extrapolated to the *aided user* measurements timestamps, before estimating the *aiding user* SPP position.

Therefore, the present section defines the pseudorange measurements, the time-compensation technique, the SPP estimation technique and all the GNSS ranging techniques that the present contribution applied to infer the Inter-Spacecraft Range (ISR) in a lunar scenario of DGNSS.

In the following, the inter-user range will be referred to as ISR or baseline length and the inter-user vector as ISV or baseline vector.

2.1.1. Pseudorange Measurements

In GNSS systems, the receivers recover their position by trilateration of the measured distances to multiple visible satellites [14,49]. These distances are derived from an estimated time of transmission and are called *pseudorange measurements*. As explained in [50], the pseudorange measurements between GNSS receiver i to satellite s at epoch k are affected by various sources of errors and can be decomposed into:

$$\rho^s_{i,k} = r^s_{i,k} + b_{i,k} - c \cdot \delta t^s_k + d_{atm,k} + \epsilon^s_{i,k} \tag{3}$$

where $r^s_{i,k}$ is the range between receiver i and satellite s, $b_{i,k} = c \cdot \delta t^r_{i,k}$ is the range offset caused by the receiver's local clock bias $\delta t^r_{i,k}$ to the system time, δt^s_k is the modeled part of the satellite clock offset with the system time, which includes the correction calculated using the values broadcast in the navigation messages (for SPP) as well as a small relativistic correction caused by the orbital eccentricity and $d_{atm,k}$ are the atmospheric delays, standing both for tropospheric and ionospheric delays. Finally, $\epsilon^s_{i,k}$ represents the unmodeled errors including receiver noise, multipath signals, orbital errors and other effects [50].

2.1.2. Extrapolation of Aiding User's Observables to the Aided User's Timestamps

It has to be noticed that both users have an independent clock such that the GNSS measurements from the aiding user are not synchronous with the GNSS measurements from the aided user. The offset between their respective measurements timestamp is $\Delta t_{ij,k} = t_{j,k} - t_{i,k}$, where $t_{*,k}$ is the receiver timestamp associated with a given set of pseudorange measurements after the correction of the corresponding receiver clock bias $\delta t^r_{*,k}$ for user $*$ (which denotes the user ID, i or j). One way to retrieve such a clock bias estimate $\delta \hat{t}^r_{*,k}$, and the one considered in the present analysis, is to estimate it via the Least Squares (LS) SPP, as will be explained in Section 2.1.3.

To compensate for this timestamp offset $\Delta t_{ij,k}$, the measurements of the aiding user have to be extrapolated at the timestamp of the aided user $t_{i,k}$. This is achieved by using, for example, the range-rate information that can be inferred by the Doppler measurements. This aspect is of particular importance in the case of a space scenario involving orbiters. Indeed, given the high user velocity, the users might have traveled a long distance over the timestamp offset $\Delta t_{ij,k}$ duration, and hence the ISR value would be affected by a significant error if no such time-alignment was performed. The technique to extrapolate the measurements of the *aiding user* to the *aided user* measurement timestamps, as introduced in [51], is based on the Doppler frequency shift of the *aiding user* j with the satellite s, $\phi^s_j(t_{j,k})$ so that

$$\begin{aligned} \hat{\rho}^s_j(t_{i,k}) &= \rho^s_j(t_{j,k} - \Delta t_{ij,k}) \\ &= \rho^s_j(t_{j,k}) - \Delta t_{ij,k} \cdot \lambda_{f_c} \cdot \phi^s_j(t_{j,k}), \end{aligned} \tag{4}$$

where λ_{f_c} is the wavelength associated with the carrier frequency of the GNSS signals, 0.2549 m for L5/E5a, being the focus frequency band of the present contribution, given its inherent advantages for spaceborne GNSS users, as discussed in [42]. L5/E5a has indeed some clear advantages given its wider transmission antenna pattern beamwidth and its lower carrier frequency when compared to E1/L1 resulting in better signal availability and lower free space path loss. Also, in the case of Global Positioning System (GPS), the L5

signal is preferred over the L1 signal given its narrower bandwidth leading to a decrease in receiver noise and an increase in ranging accuracy.

2.1.3. Single Point Position (SPP) Estimation

To proceed to the various DGNSS ranging techniques, an approximation of the involved users' position $\hat{\mathbf{x}}_{*,k}$ and local clock offset $\delta\hat{t}^{r}_{*,k} = \hat{b}_{*,k}/c$ is needed. A GNSS receiver can solve both for its own position and for the *aiding user*'s position by using the external pseudorange measurements after extrapolation to its own local timestamps. Through this approach, the exchange of the estimated position is not necessary since it can be computed locally at the aided receiver. The SPP estimate of each user is obtained thanks to an iterative LS estimator, where at each iteration l, the user assumed position $\hat{\mathbf{x}}_{*,k}$ is updated based on the linearization of the pseudorange equation with a Taylor expansion truncated at the first order:

$$\hat{\mathbf{x}}_{*,k} = \hat{\mathbf{x}}^{l-1}_{*,k} + \Delta\hat{\mathbf{x}}^{l}_{*,k} \tag{5}$$

where $\hat{\mathbf{x}}^{l-1}_{*,k}$ is the position estimated at the previous iteration for user $*$ (i or j, interchangeably) and $\Delta\hat{\mathbf{x}}^{l}_{*,k}$ is the increment in position for the current iteration l and is obtained together with the user clock bias increment $\Delta\hat{b}^{l}_{*,k}$ with:

$$\begin{bmatrix} \Delta\hat{\mathbf{x}}^{l}_{*,k} \\ \Delta\hat{b}^{l}_{*,k} \end{bmatrix} = \left(\mathbf{H}^{l\top}\mathbf{H}^{l}\right)^{-1}\mathbf{H}^{l\top}\boldsymbol{\Delta\rho}^{l}_{*,k}, \tag{6}$$

where $\mathbf{H}^{l}$ is the $N \times 4$ direction cosine matrix at iteration l estimated from the most recent estimation of the user * position. It is made of the *unit steering vectors* to the satellite s at epoch k, $\mathbf{h}^{s}_{*,k}$ [14]:

$$\mathbf{H}^{l} = \begin{bmatrix} \mathbf{h}^{1}_{*,k} & 1 \\ \mathbf{h}^{2}_{*,k} & 1 \\ \vdots & \vdots \\ \mathbf{h}^{N}_{*,k} & 1 \end{bmatrix} \tag{7}$$

$\Delta\boldsymbol{\rho}^{l}_{*,k}$ is the pseudorange increment vector $N \times 1$ which has been corrected for the last estimate of the user clock bias. N represents the number of GNSS satellites involved in the computation and must be at least equal to 4 for an unbiased estimation of the 3D user position and its clock bias.

2.1.4. Absolute Position Difference (APD)

The first technique presented in this paper is called *Absolute Positions Differencing*. This technique was considered with the same nomenclature in [23], under the name of Differential Positioning (DPOS) from single-point processing (DPOS) in [52] and also in [45]. It is based on taking the Euclidean norm of the difference of the SPP estimations of each user individually:

$$\hat{d}_{ij,k} = ||\hat{\mathbf{d}}_{ij,k}|| = ||\hat{\mathbf{x}}_{j,k} - \hat{\mathbf{x}}_{i,k}||. \tag{8}$$

This technique will be named `APD` in the results presented in Section 4. A technique similar to APD was described in the literature in [23,45] and was called *Pseudorange Ranging*. This technique works by performing a joint estimation of both users' state vectors within the same equation by superimposing the normal equations of the two. This technique was tested but not reported in the present contribution as it did not show added value with respect to APD.

2.1.5. Single Differences Ranging

Also based on the exchange of the set of pseudorange measurements from the aiding to the *aided user*, this technique exploits a set of differential quantities known as Single Differences (SD). It was introduced in [53,54]. A generic SD can be defined

between two GNSS receivers, i and j tracking a common satellite s as the difference between synchronous pseudorange measurements:

$$\begin{aligned} S^s_{ij,k} &= \rho^s_{j,k} - \rho^s_{i,k} \\ &= \Delta r^s_{ij,k} + \Delta b_{ij,k} + \Delta \epsilon_{ij,k}, \end{aligned} \tag{9}$$

where $\Delta r^s_{ij,k}$ is the difference between the ranges from the i-th and j-th users to satellite s, $\Delta b_{ij,k}$ is the difference between the clock biases of the two users and $\Delta \epsilon_{ij,k}$ is a noise term that aggregates all the non-correlated errors. In fact, provided that all the measurements are synchronous, SDs allow canceling satellite clock errors as well as the part of the satellite orbital errors common to both users and the other correlated bias terms affecting pseudorange measurements. Besides the cancellation of correlated error terms, the variance in the uncorrelated errors, such as thermal noise, is increased. These noise contributions are hence aggregated in $\Delta \epsilon_{ij,k}$. Assuming a minimum of four visible GNSS satellites common to both users, the computation of the baseline vector based on SD is performed through:

$$\begin{bmatrix} S^1_{ij,k} \\ S^2_{ij,k} \\ \vdots \\ S^S_{ij,k} \end{bmatrix} \simeq - \begin{bmatrix} \mathbf{h}^1_{*,k} & 1 \\ \mathbf{h}^2_{*,k} & 1 \\ \vdots & \vdots \\ \mathbf{h}^S_{*,k} & 1 \end{bmatrix} \begin{bmatrix} \mathbf{d}_{ij,k} \\ \Delta b_{ij,k} \end{bmatrix} \tag{10}$$

where $*$ represents the point chosen as the origin for the unit steering vector, which could be the SPP estimate of the *aided user*, *aiding user*, or a higher quality estimation from one of the user's positions. By means of this approach, the exchange of the estimated position is not necessary since it can be computed autonomously at the aided receiver. The current contribution presents, therefore, a comparison of the different cases to understand the impact of the linearization point accuracy on the final ISR estimation. The Section 4 shows an assessment of the baseline estimation quality as a function of this chosen point. This technique will be named SD $\mathtt{H_{aiding}}$ and SD $\mathtt{H_{aided}}$ when the *aiding user* and the *aided user*, respectively, are used as origins of the steering vectors in the results presented in Section 4.

2.1.6. Double Differences Ranging

This technique was introduced in [53–55]. When the same pair of satellites r and s are visible to both receivers, a Double Differences (DD) measurement can be obtained as the difference of two SDs:

$$D^{sr}_{ij,k} = S^s_{ij,k} - S^r_{ij,k} = \Delta R^{sr}_{ij,k} + \Sigma_{ij,k}, \tag{11}$$

where S^s_{ij} is an SD computed according to Equation (9), $S^r_{ij,k}$ is an SD taken with respect to a satellite chosen as reference for the DD algorithm, while Σ_{ij} is a random variable collecting residual error contributions that cannot be canceled due to the non-correlation between the measurements such as multipath, second-order noise components of the receiver front-ends and residual, unmodeled noise contributions [14]. However, DDs allow the cancellation of:

- the differential clock bias $\Delta b_{ij,k}$ between the cooperating users when uncorrected pseudoranges are used,
- or the differential residual error on the clock bias estimation when pseudoranges corrected from the estimated receiver clock bias are used $\Delta b_{ij,k}$.

The term ΔR^{sr} can be expressed highlighting the dependency from the baseline vector as:

$$\Delta R^{sr,k} = \left[\mathbf{h}^r_{*,k} - \mathbf{h}^s_{*,k} \right]^T \mathbf{d}_{ij,k}. \tag{12}$$

This technique will be named DD $\mathtt{H_{aiding}}$ and DD $\mathtt{H_{aided}}$ when the *aiding user* and the *aided user*, respectively, are used as origins of the steering vectors in the results presented in Section 4.

2.2. Characteristics of a Space DGNSS Scenario

2.2.1. Measurements Errors

When transitioning to a lunar GNSS scenario, the pseudorange model described in Equation (3) can be simplified. This section explains the main differences between a terrestrial and a lunar GNSS scenario as well as the potential obstacles for DGNSS ranging in space with respect to the GNSS measurements considered in this study.

Atmospheric delays

The typical atmospheric delays considered in GNSS navigation, being the tropospheric and ionospheric delays, and represented by $d_{atm,k}$ in Equation (3) become less of a concern as most of the GNSS signals received at lunar altitudes did not propagate through these layers. This is due to the GNSS constellations' altitude being significantly higher than the upper limit of the Earth's ionosphere combined with the fact that the lunar GNSS users are located even higher than the GNSS constellations themselves. As a consequence, a GNSS user located in space and above the GNSS constellations typically receives GNSS signals transmitted by satellites on the other side of the Earth relative to the user's location as well as from the side. However, it will not be able to track signals from the closest transmitting satellites, as GNSS antenna patterns are pointing toward the center of the Earth. This becomes obvious when looking at Figure 2, where the ionosphere and its upper limit are depicted in orange. This has already been thoroughly analyzed and discussed in [42], which analyzes the off-boresight angles histogram of the Galileo and GPS signals which are actually tracked by a GNSS receiver simulated in the lunar Gateway orbit. It shows that over a one-week simulated period of a GNSS receiver in lunar orbit, more than 80% of the signals tracked by this lunar receiver originate from the side lobes of the transmitting satellites' antenna. Concerning the main lobe, over the 8.3° of angle aperture not covered by the Earth's body, only 2° are covered by the ionosphere, as depicted in Figure 2. A mask can hence be applied to discard the few satellites of which the signals actually crossed the ionosphere by setting a conservative upper ionosphere's limit such as 1000 km as considered in [56]. They will, therefore, be omitted in the following analyses.

Signal In Space Error (SISE)

For a GNSS receiver in lunar orbit, the C/N_0 of the signals tracked are low and highly variable [41]. This implies a reduced capacity of the receiver to demodulate the navigation message as demonstrated in [42], which shows a significant reduction in the visibility of a GNSS receiver in lunar orbit when the navigation message can not be demodulated versus when it can be. More specifically, the analyses performed in [42] showed that the GPS L1 signal ephemerides can be demodulated for only 5 to 40% of the time over the one-week simulated period of a GNSS receiver in lunar orbit. Hence, given the potential capacity overload of the ground network of deep space antennas, the receiver must be capable of using ephemerides demodulated in the past, i.e., with an older age of data. As a consequence, this might increase the GNSS satellite orbit residual errors significantly with respect to terrestrial applications. These are characterized by SISE that is defined as the difference of the satellite position and time as broadcast by the navigation message and the true satellite position and time, projected on the user-satellite direction [57]. In Equation (3), they are hidden in the unmodeled errors term $\epsilon^s_{i,k}$. They remain under 1 m for ground applications as stated in [49]. In [57], the characterization of the SISE 95% was performed for GPS over 4 years in the nominal range of the navigation message age of data (<3 h). However, outside of this nominal range, as explained in [58], the globally averaged SISE orbit degrades gracefully over time and is specified to remain below a 95th-percentile value of 388 m throughout a two-week period. Therefore, as a worst-case scenario, satellite orbital errors with a norm of 400 m of which the direction is randomly generated and follows a normal distribution are considered in this contribution. The objective of considering this worst-case scenario is to assess the potential of DGNSS techniques to cancel the effect of GNSS orbital errors despite the large ISR values, resulting in the decorrelation of the Signal In Space Ranging Error between the two users.

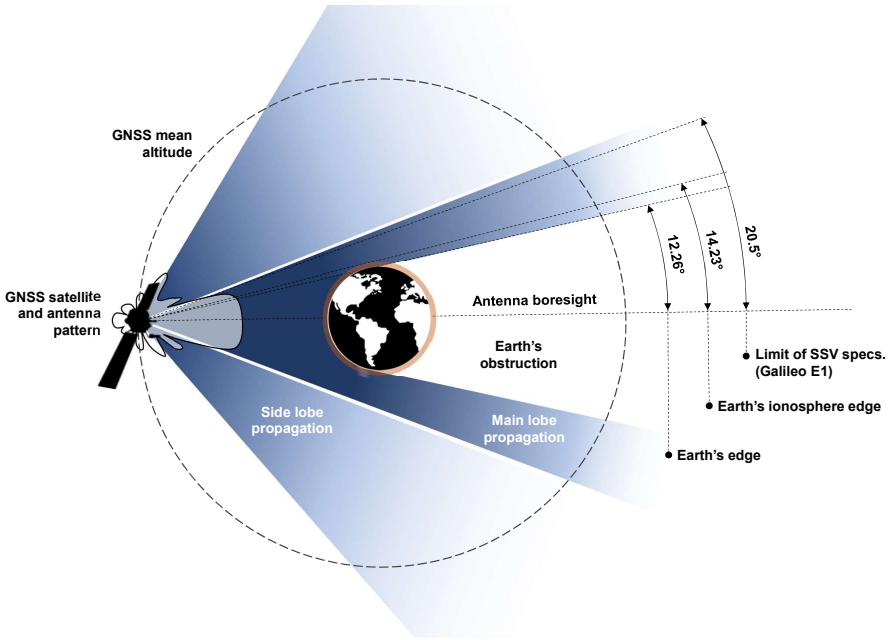

Figure 2. Schematic of the GNSS transmitted signals in deep space. The main lobe beamwidth value was taken from the interoperable GNSS SSV book [8].

Inter-user measurements alignment

In Section 2.1.2, the observables alignment technique was presented assuming that the receiver timestamps after clock bias correction, $t_{i,k}$ and $t_{j,k}$, are perfectly known. However, in real GNSS scenarios, $\hat{t}_{*,k}$ is estimated based on the prior estimation of the receiver clock bias $\hat{b}_{*,k}$. The quality of these estimates hence depends on the satellite visibility and the GDOP [14,49,50,59]. And as already shown in [42], in lunar GNSS scenarios, the visibility of the satellites is low and the DOP values are high. As a consequence, in a lunar DGNSS scenario, the inter-user measurements time-offset estimates $\Delta\hat{t}_{ij,k}$ might be affected by significant residual errors. Given the high user velocities characteristic of lunar orbiters, a small error in timestamp offset estimation can result in a large error in ISR estimation as the pseudoranges of the aiding user would be interpolated at a slightly erroneous point in time, using Equation (4). Additionally, as space GNSS users are characterized by larger Doppler shifts when compared to terrestrial users, a small estimation residual error left on $\Delta\hat{t}_{ij,k}$ would result in a larger time-compensation error when compared to a terrestrial scenario.

2.2.2. Parallelism Assumption Used for Terrestrial Applications

In a lunar DGNSS scenario, the ISR can become significantly large with respect to the ranges separating the users from the GNSS satellites in contrast to a terrestrial DGNSS scenario. This difference can impact the performance of DGNSS ranging in space. The present section presents these differences, exposes the inherent issues and proposes potential solutions.

Definition of the bias introduced by the parallelism assumption

On top of the measurements modeling differences explained in the previous section, the performances of DGNSS in space are also subject to variations with respect to the performances presented for terrestrial applications. This is due to the assumption taken to establish the relationship presented in Equation (13). Indeed, as stated in [23,39,40,44,60], the system of equations presented in Equation (10) comes from the assumption that the difference in true ranges $\Delta r^s_{ij,k}$ can be approximated by the inner product between the

baseline vector $\mathbf{d}_{ij,k}$ and the unit steering vector $\mathbf{h}^s_{i,k}$ or $\mathbf{h}^s_{j,k}$ between either user i or j and the satellite s.

$$\Delta r^s_{ij,k} \approx -\left[\mathbf{h}^s_{*,k}\right]^T \mathbf{d}_{ij,k} \tag{13}$$

This operation is depicted in Figure 1a, in which the projection of the baseline vector $\mathbf{d}_{ij,k}$ on the direction $\mathbf{h}^s_{*,k}$ is exactly equal to the difference in true ranges $\Delta r^s_{ij,k}$. This assumption holds while the true ranges $r^s_{i,k}$ and $r^s_{j,k}$ from satellite s to users i and j are much larger than the distance $d_{ij,k}$ between i and j, where in such a case their respective unit steering vector $\mathbf{h}^s_{i,k}$ and $\mathbf{h}^s_{j,k}$ are nearly parallel to each other, as depicted in Figure 1a.

However, the typical distances of a DGNSS scenario for spaceborne users are easily two orders of magnitudes larger than for terrestrial applications. Hence, this parallelism assumption is likely to introduce a bias in the ISR estimation process, as initially presented in [61] for long baseline Doppler positioning based on Signal of Opportunity (SoP) from LEO. As depicted in Figure 1b, when the distance between the users and the navigation satellites is not large enough with respect to the baseline length for the unit steering vectors originating from both users to be considered parallel, a bias term $\varepsilon(\Delta r^s_{ij,k})$ is introduced:

$$\Delta r^s_{ij,k} = -\left[\mathbf{h}^s_{*,k}\right]^T \mathbf{d}_{ij,k} + \varepsilon_*(\Delta r^s_{ij,k}), \tag{14}$$

where, if the unit steering vectors from the *aided user* $\mathbf{h}^s_{i,k}$ are used in the SD LS $\mathbf{H}$ design matrix, the bias term can be written as

$$\begin{aligned} \varepsilon_i(\Delta r^s_{ij,k}) &= r^s_{i,k} - r^s_{j,k}\left[\mathbf{h}^s_{j,k}\right]^T\left[\mathbf{h}^s_{i,k}\right] + \Delta r^s_{ij,k} \\ &= r^s_{j,k} - r^s_{j,k}\left[\mathbf{h}^s_{j,k}\right]^T\left[\mathbf{h}^s_{i,k}\right] \\ &= r^s_{j,k}(1 - \left[\mathbf{h}^s_{j,k}\right]^T\left[\mathbf{h}^s_{i,k}\right]). \end{aligned} \tag{15}$$

If this correction term Equation (15) is inserted directly in Equation (14) after the replacement of:

- unknown ranges $r^s_{j,k}$ by the corrected pseudoranges $\hat{\rho}^s_{corr,j,k}$ from the SPP estimate and,
- the range differences $\Delta r^s_{ij,k}$ by the SD measurements $S^s_{ij,k}$,

a new equation can be obtained:

$$S^s_{ij,k} - \hat{\rho}^s_{corr,j,k}(1 - \left[\mathbf{h}^s_{j,k}\right]^T\left[\mathbf{h}^s_{i,k}\right]) = -\left[\mathbf{h}^s_{*,k}\right]^T \mathbf{d}_{ij,k} + \Delta b_{ij,k}, \tag{16}$$

and replaced in Equation (10). This technique will be named $\texttt{SD H}_{\texttt{aided,corrected}}$ in the results presented in Section 4.

Redefinition of the unit steering vectors for the space scenario

Another proposed solution, that takes into account the invalidity of the parallelism assumption for space scenarios, while keeping the algorithm linear for its low-complexity advantage, is to redefine the unit vectors considered in the design matrix $\mathbf{H}$ from Equation (10). Instead of using either $\mathbf{h}^s_{i,k}$ or $\mathbf{h}^s_{j,k}$, a combination of both based on their normalized sum can be used:

$$\mathbf{h}^s_{i+j,k} = \frac{\mathbf{h}^s_{i,k} + \mathbf{h}^s_{j,k}}{||\mathbf{h}^s_{i,k} + \mathbf{h}^s_{j,k}||}. \tag{17}$$

Consequently, the difference in true ranges changes with respect to Equation (13) and it becomes:

$$\Delta r^s_{ij,k} \approx -\left[\mathbf{h}^s_{i+j,k}\right]^T \mathbf{d}_{ij,k}. \tag{18}$$

This technique will be named `SD Hsum`, or `DD Hsum`, if the unit vectors Equation (17) are replaced in Equation (12), in the results presented in Section 4.

Finally, another solution presented in the literature in the context of differential Doppler positioning in [61], consists in finding the unit steering vector $\mathbf{h}^s_{ideal,k}$, which at each epoch k will satisfy exactly Equation (13), such that:

$$\Delta r^s_{ij,k} = -\left[\mathbf{h}^s_{ideal,k}\right]^T \mathbf{d}_{ij,k}. \tag{19}$$

The angle α_k between $\mathbf{h}^s_{ideal,k}$ and $\mathbf{d}_{ij,k}$ is given by:

$$\cos(\alpha_k) = -\frac{\Delta r^s_{ij,k}}{d_{ij,k}}, \tag{20}$$

where $\mathbf{h}^s_{ideal,k}$ satisfying this condition form a conical surface. A solution consists of defining the vector $\mathbf{h}^s_{\perp,k}$ normal to both $\mathbf{d}_{ij,k}$ and $\mathbf{h}^s_{i,k}$:

$$\mathbf{h}^s_{\perp,k} = \frac{\mathbf{h}^s_{i,k} \times \mathbf{d}_{ij,k}}{||\mathbf{h}^s_{i,k} \times \mathbf{d}_{ij,k}||}, \tag{21}$$

and then to apply Rodrigues' rotation formula to obtain $\mathbf{h}^s_{ideal,k}$ in the plan that contains both $\mathbf{d}_{ij,k}$ and $\mathbf{h}^s_{i,k}$ by rotating the baseline unit vector $\mathbf{h}^s_{ij,k}$ around $\mathbf{h}^s_{\perp,k}$ by the angle α_k according to the right-hand rule:

$$\begin{aligned} \mathbf{h}^s_{ideal,k} &= \mathbf{h}^s_{ij,k}\cos(\alpha_k) + (\mathbf{h}^s_{\perp,k} \times \mathbf{h}^s_{ij,k})\sin(\alpha_k) + \\ &\quad \mathbf{h}^s_{\perp,k}(\mathbf{h}^s_{\perp,k} \cdot \mathbf{h}^s_{ij,k})(1 - \cos(\alpha_k)) \\ &= \mathbf{h}^s_{ij,k}\cos(\alpha_k) + (\mathbf{h}^s_{\perp,k} \times \mathbf{h}^s_{ij,k})\sin(\alpha_k). \end{aligned} \tag{22}$$

Consequently, these newly defined unit vector $\mathbf{h}^s_{ideal,k}$ for the differential LS problem can replace $\mathbf{h}^S_{i,k}$ in the $\mathbf{H}$ design matrix of Equations (10) and (12). These two techniques will be named `SD Hideal`, or `DD Hideal` in the results presented in Section 4.
All the above-described models will be compared to identify the best solution for DGNSS ranging in space.

Satellite orbital errors cancelling potential in space

As mentioned above, the closer the parallelism assumption is to reality, the better the performances of the ISR estimator in terms of bias. This statement is true not only for the bias introduced by Equation (13) but also for the residual GNSS satellites orbital errors. Indeed, the capacity of the differential GNSS algorithms to cancel orbital errors depends on the angle between the steering vectors from the two users to a given GNSS satellite. Given the large orders of magnitude for a lunar differential GNSS scenario using Earth GNSS signals, it is of interest to understand how well the application of DGNSS for lunar orbiters can remove orbital errors. To this end, the angles $\theta^s_{ij,k}$ as depicted in Figure 1b will be displayed over time as well as the residual on the orbital errors $\Delta e^s_{LOS,ij,k}$ after application of single differencing on the pseudorange observables. Its value is computed according to:

$$\Delta e^s_{LOS,ij,k} = ||\boldsymbol{e}^s_k||(\cos\beta^s_{i,k} - \cos(\theta^s_{ij,k} + \beta^s_{i,k})), \tag{23}$$

where $\beta^s_{i,k}$ is the angle between the GNSS satellite position error vector $\boldsymbol{e}^s_k$ and the unit steering vector from the *aided user* $\boldsymbol{h}^s_{i,k}$.

3. Methodology

3.1. The Lunar Orbiter Scenarios

3.1.1. Presentation

In order to analyze the applicability of the concept in space, a scenario including two lunar missions foreseen in the next years has been taken as a meaningful example. The estimation of the baseline length is performed between a lunar CubeSat, Volatile and Mineralogy Mapping Orbiter (VMMO), and the communication relay Lunar Pathfinder (LPF). Both mission trajectories have been obtained based on an initial state found in the literature and propagated with the High-Precision Orbit Propagator (HPOP) of STK [62]. The force model applied to propagate the initial state considers the Moon as a central body using a maximum degree and a maximum order of geopotential coefficients of 48 to be included for gravity computations. The gravity file 'GL0660B.grv' from the GRAIL mission was used [63]. The Earth and the Sun were considered as point masses and the STK default SRP model was applied. A representative orbit for the VMMO mission consists in the Low Lunar Frozen Orbit (LLFO) of which the keplerian parameters are reported in [64].

The second lunar mission considered in this paper, the LPF, is planned to fly to the Moon in an Elliptical Lunar Frozen Orbit (ELFO) [6,65]. The goal of this mission is to serve as a relay between lunar assets via the S-band and Earth in the X-Band [66]. The orbit of LPF favors a long-duration coverage of the lunar southern hemisphere attractive for early lunar missions, and its orbital keplerian parameters are given in [65]. It covers the far side of the Moon and benefits from long access times to Earth to relay back customers' data, which will also benefit its GNSS visibility.

The overall scenario is depicted in Figure 3. This scenario is a potential real scenario as these two missions will both have a GNSS receiver aboard and a communication link to communicate with neighboring space missions. This scenario is simulated on 09-Nov-2025 00:00:00.000 Coordinated Universal Time (UTC) when the presence in space of both user missions can be assumed. The VMMO and Pathfinder were chosen as potential users for three reasons. The first is related to the certitude that they will both fly soon into space, with a planned date in 2025 [6,67]. The second is that Lunar Pathfinder will be one of the two very first missions ever to fly a Galileo-GPS receiver onboard all the way to the Moon, and will return GNSS Doppler, Pseudoranges, and Carrier Phase measurements as well as signal samples back to the ground. Finally, the CubeSat was an ideal candidate for presenting this concept given its low-cost constraint that justifies a potential need for low-complexity ranging techniques.

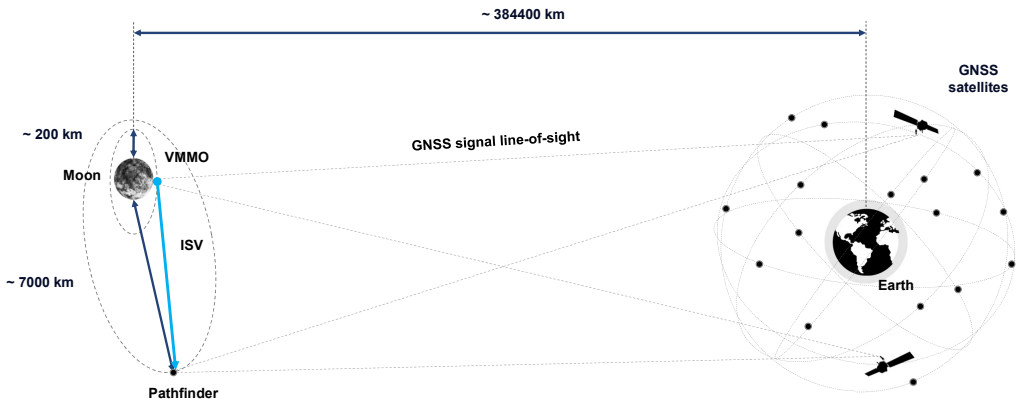

Figure 3. Schematic of the GNSS scenario for VMMO and Pathfinder.

3.1.2. Comparison with a Terrestrial Scenario

To compare the parallelism assumption validity in a terrestrial scenario with respect to the space scenario of Figure 3, the ratio between the inter-users distance $d_{ij,k}$, as shown

in Figure 4, and a typical user-to-satellite range $r^s_{*,k}$ is considered. The closer this ratio is to zero, the closer the assumption is to be valid. Table 1 presents typical values of this ratio in a terrestrial case with respect to the lunar scenario, considering the distances typical to the VMMO-Pathfinder cooperation and the GPS constellation. The numbers shown in Table 1 show that in a DGNSS case applied to a typical lunar scenario, the ratio becomes significantly higher when compared to terrestrial applications. In the long-baseline DGNSS terrestrial applications presented in the literature, the dominant error factor becomes the ionospheric and tropospheric delays between the cooperating users such that the effect of the bias introduced by the assumption in Equation (13) in the algorithm itself is not analyzed [68–70].

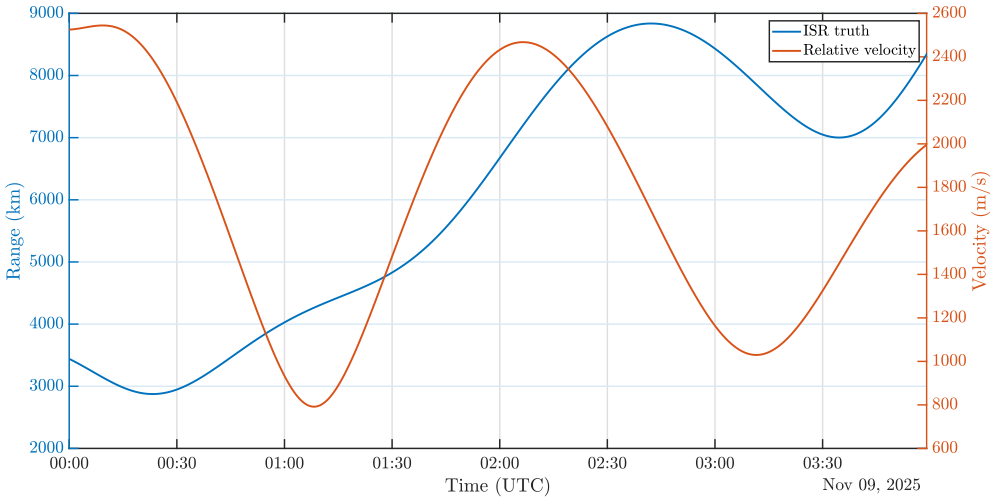

Figure 4. ISR and relative velocity between VMMO and Pathfinder over a 4 h test window.

Table 1. Comparison of the parallelism assumption validity between terrestrial and lunar scenarios.

Typical Values	Terrestrial Scenario [16,68]	Lunar Scenario
Inter-user range (km)	[0; 300]	[2500; 11,000]
User-to-satellite distance (km)	20,200	380,000
Validity ratio (‰)	[0; 15]	[6; 29]

On top of the introduction of a bias due to the large ISR values, Figure 4 also confirms that such a differential scenario in space is also characterized by large relative velocities between the involved users, as anticipated in Section 2.2.1. This causes the ISR variation rate to be large. Consequently, a residual error on the aiding user's observables extrapolation process might be more impactful on the final ISR estimation quality, when compared to terrestrial scenarios. The significant user dynamics also cause high pseudorange rates and hence high Doppler shift values. Figure 5 shows the Doppler shifts of the GNSS signals received by Pathfinder, with values up to 17 kHz when compared to around 2 kHz for typical terrestrial ground users. As a consequence, a residual error on the estimated time offset between a pair of measurements used for differential algorithms is likely to be amplified by the large Doppler shifts characteristic of lunar GNSS users.

Figure 6 shows the GDOP and the visibility of the number of common GNSS signals acquired by both receivers, meaning the signals of which the C/N_0 are higher than the receiver sensitivity. Figure 7 shows the C/N_0 of the signals tracked by a simulated receiver in lunar orbit (VMMO) as simulated by STK. The formula used to calculate these values is to be found in [42]. And finally, Figure 8 represents the angle θ^s_{ij}, as depicted in Figure 1b between the two Line-of-Sight (LoS) vectors between each user and the GNSS satellite, for each visible GNSS satellite s over time, in parallel with the ISR truth. As expected, it shows that there is a high correlation between the ISR truth and the invalidity of the parallelism

assumption. As opposed to a ground terrestrial application, however, it can happen for such a 3D scenario that the baseline is relatively long, i.e., >4000 km after 01:00 a.m., while the angles stay relatively small, <0.1 deg, as it is the case when the two end users are aligned with the Earth position.

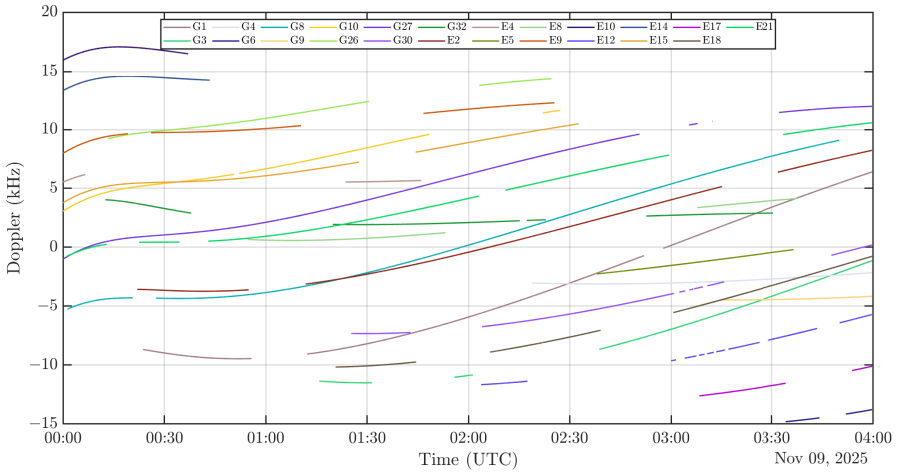

Figure 5. Doppler shifts between Pathfinder and the GNSS satellites over a 4 h test window.

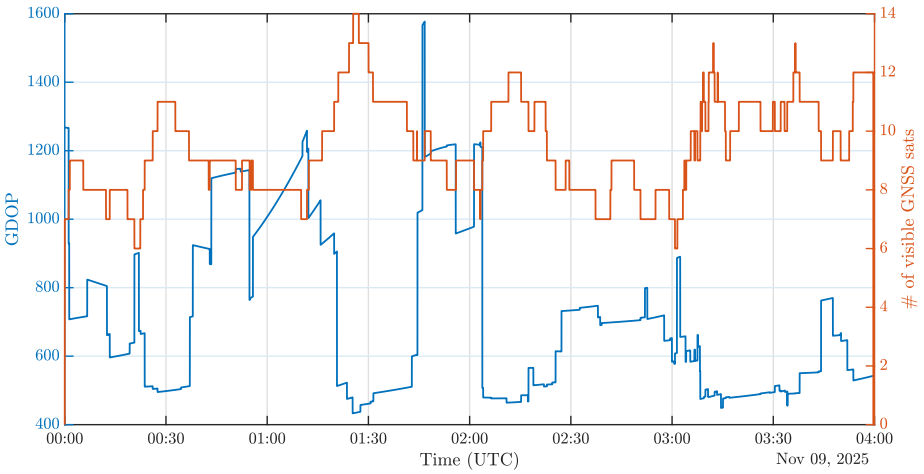

Figure 6. DOP and Visibility of common GNSS satellites.

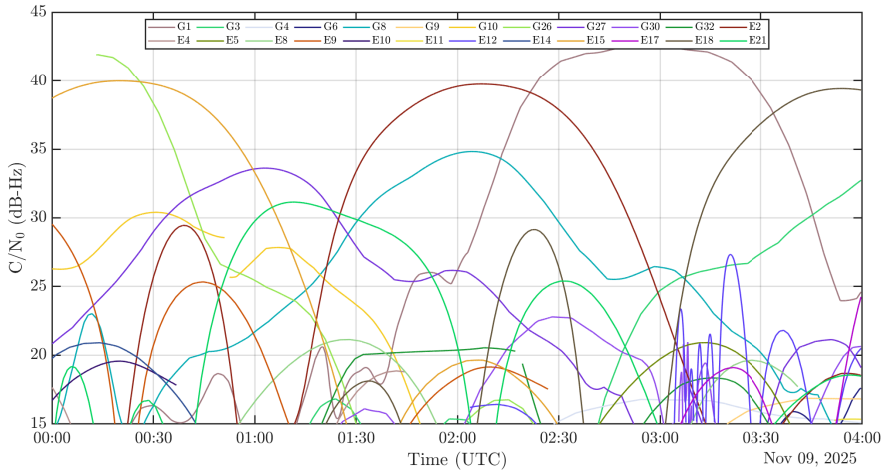

Figure 7. C/N_0 tracks of the VMMO mission.

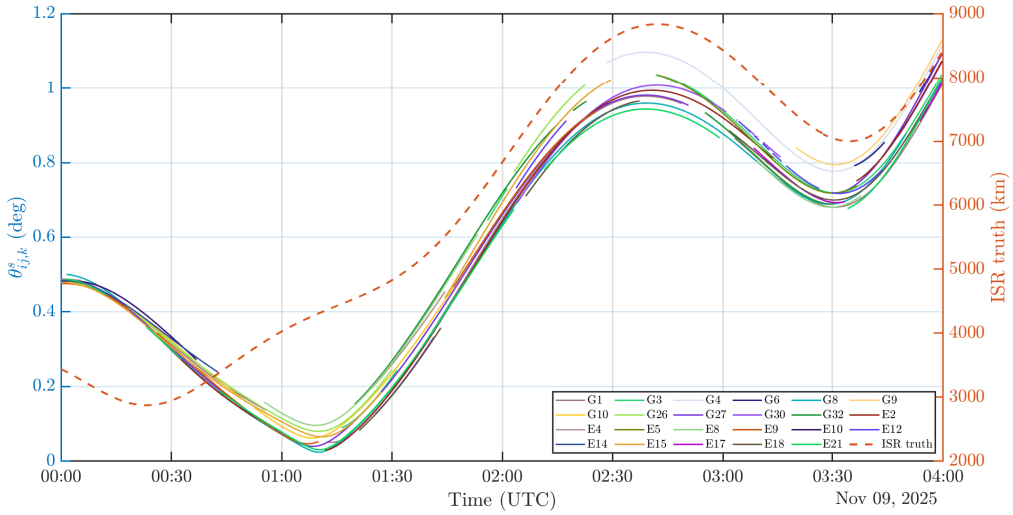

Figure 8. Inter steering vectors angles.

3.2. Simulation Scenario: Monte Carlo

To assess the performances of GNSS ranging for a lunar scenario, two types of environments have been set up enabling both theoretical as well as experimental analyses. The first setup resorts to a Monte Carlo analysis implemented in Matlab on measurements extracted from STK while the second is based on the measurements made by a real spaceborne receiver that simulates the reception of GNSS signals in lunar orbit. Both environments use exactly the same scenario at the same epoch and for the same duration, on the 9 November 2025 00:00:00.000 UTC for a duration of four hours for comparison purposes. While the experimental environment is based on the actual NaviMoon spaceborne receiver in a HWiL architecture, the theoretical simulation is modeling a receiver based on the NaviMoon parameters [71]. Namely, the considered receiver sensitivity is 15 dB-Hz. The theoretical simulations allows to individually assess specific factors involved in the ISR estimation process of a space scenario, by isolating the source of errors one by one.

The scenario described in Section 3.1 was created using STK. The ephemerides used for the Galileo and GPS constellations were obtained from SpacePNT and contained 21 and 32 satellites, respectively. The antenna patterns for GPS were obtained online from the U.S. Navigation Center [72] while the Galileo patterns were obtained internally at ESA. L5/E5a is the focus frequency band of the present contribution, given its inherent advantages for spaceborne GNSS users, as discussed in [42]. The user's trajectories were obtained in STK by giving it an initial state vector and propagating it with its high-fidelity orbit propagator to generate the reference trajectories of the VMMO and of the LPF. Once the ranges, spacecraft positions and C/N_0 levels are extracted from STK, these data are then post-processed in Matlab to characterize the quality of the ISR estimator.

The C/N_0 levels are converted to pseudorange standard deviations based on the Betz theory, providing an estimation of the code tracking accuracy as a function of the RF front-end parameters and the C/N_0 [73]. The pseudorange noise is then generated for each Monte Carlo simulation. The receiver's local clock biases are set with values observed during the NaviMoon experiments in the laboratory. The clock bias and position of each orbiter are then estimated individually. The time series of each user is then corrected based on the estimated clock bias. The measurements of the *aiding user* are then time-compensated to match the respective closest timestamps of the *aided user*, according to Equation (4). Finally, the ISR are estimated based on the set of visible GNSS satellites common to both users.

3.3. Experimental Environment: NaviMoon Spaceborne Receiver

For the HWiL case, the three segments of a GNSS positioning scenario followed by a post-processing phase are emulated, as represented on the block diagram of Figure 9.

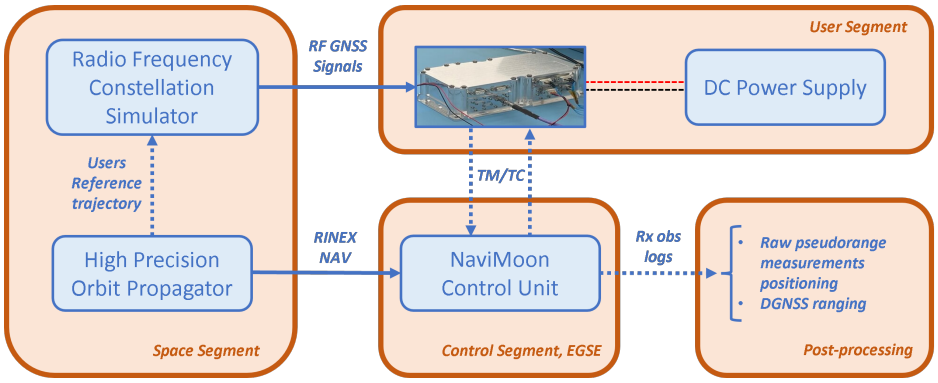

Figure 9. Test bench block diagram.

3.3.1. User Segment

The user segment made up of the NaviMoon receiver is then set up to run an aided GNSS scenario fed with an RF cable from the Spirent Radio Frequency Constellation Simulator (RFCS) generated signals. The NaviMoon is now a Technology Readiness Level (TRL) 8 technology developed by SpacePnt as its Protoflight Model has been delivered at SSTL for integration into the Lunar Pathfinder [74]. An engineering model version of the receiver is in the Radio Navigation Laboratory of ESA and it was used to perform the present tests. The NaviMoon receiver is a high-sensitivity spaceborne receiver with an acquisition engine sensitivity as low as 18 dB-Hz and a tracking threshold of 15 dB-Hz on L1/E1 and 12 dB-Hz on L5/E5a [75]. Aided data can be provided to the receiver to search only geometrically visible satellites, predict Doppler and prioritize satellites with a high C/N_0. To simulate a GNSS receiver in lunar orbit both for VMMO and Pathfinder, the following data has to be retrieved and provided to the NaviMoon as inputs:

- The initial position state of the user trajectory in Earth Centered Earth Fixed (ECEF) coordinates acting as the coarse PVT solution,
- the initial estimated clock drift of the NaviMoon clock after prior calibration on a terrestrial GNSS scenario,
- the Receiver Independent Exchange Format (RINEX) Navigation file including the GNSS constellations parameters after extraction from the RFCS.

The receiver antenna pattern is an omnidirectional pattern with a 0 dB antenna gain. The necessary power gain to complete the link budget to meet descent visibility is set on the system side. It is assumed that this would not cause a significant difference in the performances with respect to the real scenario given the fact that the intended high-gain 14 dBi Harp antenna will be steerable and have a relatively flat antenna gain over the beamwith covering the Earth GNSS satellites directions as seen by the lunar orbiter [76].

3.3.2. Space Segment and Control Segment

The same GNSS antenna patterns, ephemerides and user ground truths as for the Monte Carlo simulations were used and injected in a GNSS RFCS to create representative signals for a user in lunar orbit. The space segment of the simulated scenario is run by the ESA Radio Navigation Laboratory's RFCS. No tropospheric nor ionospheric errors were applied since the percentage of Earth GNSS signals acquired at the Moon that passes through the Earth's atmosphere is actually negligible. The GNSS transmit power levels were calibrated to match the C/N_0 levels obtained via STK, see Figure 7. The control segment communicates with the NaviMoon receiver using Telemetry and Telecommand (TM/TC) to provide the receiver with the necessary aiding and to retrieve and store the GNSS observable measurements. Finally, the post-processing block runs a positioning algorithm based on the receiver raw measurements logs and tests the various glsGNSS ranging techniques.

3.4. ISR's Key Performance Indicator

To characterize the quality of the ISR estimator as a function of the technique used in such a non-stationary process, the empirical Cumulative Distribution Function (eCDF) of the following error metrics taken at each epoch is considered. First, as a bias introduced by the violation of the parallelism assumption in the case of lunar orbiters is expected, the eCDF of the mean error at each time epoch, and hence at each baseline length, is considered:

$$\mu_{\epsilon_k}\left(\hat{d}_{ij}\right) = \frac{\sum_{n=1}^{N_{MC}}\left(\hat{d}_{ij,k,n} - d_{ij,k}\right)}{N_{MC}}, \tag{24}$$

where N_{MC} is the number of Monte Carlo simulations performed. Equation (24) can be seen as the eCDF of the bias for each stationary process of the ISR estimation at a fixed baseline. Subsequently, the standard deviation is considered in the same way in order to understand how the variances of the pseudoranges set of each user combine with one another depending on the technique:

$$\sigma_{\epsilon_k}\left(\hat{d}_{ij}\right) = \sqrt{\frac{\sum_{n=1}^{N_{MC}}\left(\hat{d}_{ij,k,n} - \mu_{\epsilon_k}\right)^2}{N_{MC}}}. \tag{25}$$

Finally, to consider a metric that summarizes the behavior of the presented linear ISR estimator, the Root Mean Square Error (RMSE) is considered.

$$\mathrm{RMSE}_{\epsilon_k}\left(\hat{d}_{ij}\right) = \sqrt{\frac{\sum_{n=1}^{N_{MC}}\left(\hat{d}_{ij,k,n} - d_{ij,k}\right)^2}{N_{MC}}}. \tag{26}$$

4. Results

4.1. ISR Estimation

As one of the main goals of this contribution is to individually assess the feasibility of GNSS-based ISR estimation in a lunar scenario despite the large-scale geometry involved, presented in Figure 4, the first set of graphs in Figure 10 represents a case where both users have perfectly synchronized measurements and are not impacted by significant systematic errors. In particular, Figure 10a shows the bias over Monte Carlo simulations performed at each epoch. As anticipated in Section 2.2.2, it shows a clear correlation between the ISR values estimated following the terrestrial parallelism assumption, that is $\mathtt{SD\ H_{aiding}}$, $\mathtt{DD\ H_{aiding}}$, $\mathtt{SD\ H_{aided}}$, $\mathtt{DD\ H_{aided}}$, and the actual angles between steering vectors. Indeed, as anticipated by analyzing Figure 8, the global minimum happens between 01:00 am and 01:30 am and the global maximum between 02:30 am and 03:00 am, reaching values of 1000 km. These results also indicate that in a lunar DGNSS ranging scenario based on the terrestrial DGNSS ranging algorithms, the minimum achievable error is around km-level. This confirms that the usual DGNSS SD and DD algorithms are not applicable as such in a space scenario. Moreover, the graph shows that no matter the linearization point chosen for creating the design matrix of the terrestrial SD algorithm, the bias magnitude remains constant, as proven by the overlapping of the curves $\mathtt{SD\ H_{aided}}$ and $\mathtt{SD\ H_{aiding}}$ as well as the overlap of the curves $\mathtt{DD\ H_{aided}}$ and $\mathtt{DD\ H_{aiding}}$, respectively, based on Equations (10) and (12) but where one is using the SPP estimate of the *aided user* as linearization point and the other is using the *aiding user*'s SPP estimate. The comparison between the SD and DD groups also manifests an increase in the introduced bias when applying the differencing operations twice, as indicated by the higher errors for DD techniques. However, it can be seen how much updating the design matrix for the ISR estimation problem, as per Equation (17) can reduce the bias initally introduced by the violation of the parallelism assumption in such geometrical configuration. As a matter of fact, the bias is reduced up to three orders of magnitude as can be observed by the transition from the $\mathtt{DD\ H_{aiding/aided}}$ results to $\mathtt{DD\ H_{sum}}$

results around 00:20 . As also shown by this figure, the estimators `SD H`$_{\texttt{ideal}}$`, DD H`$_{\texttt{ideal}}$`, APD` and `SD H`$_{\texttt{aided,corrected}}$ are actually unbiased, as expected, according to Section 2.

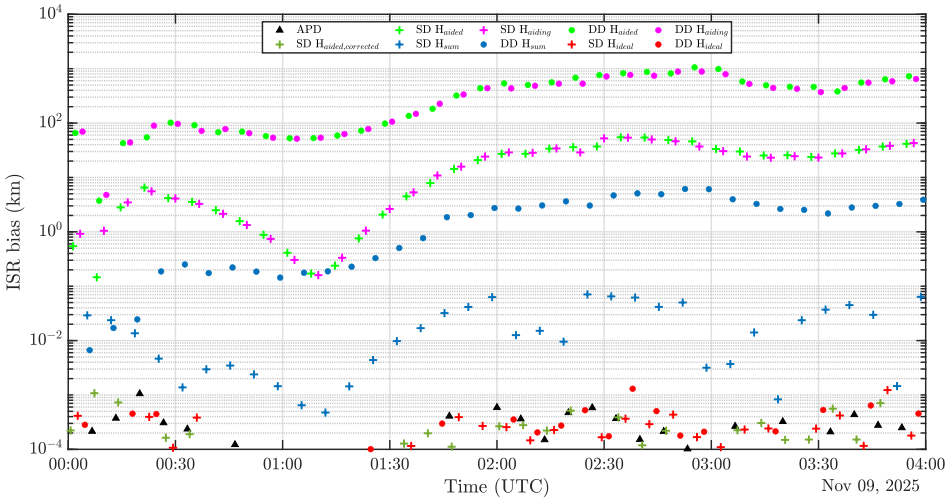

(**a**) ISR bias over time.

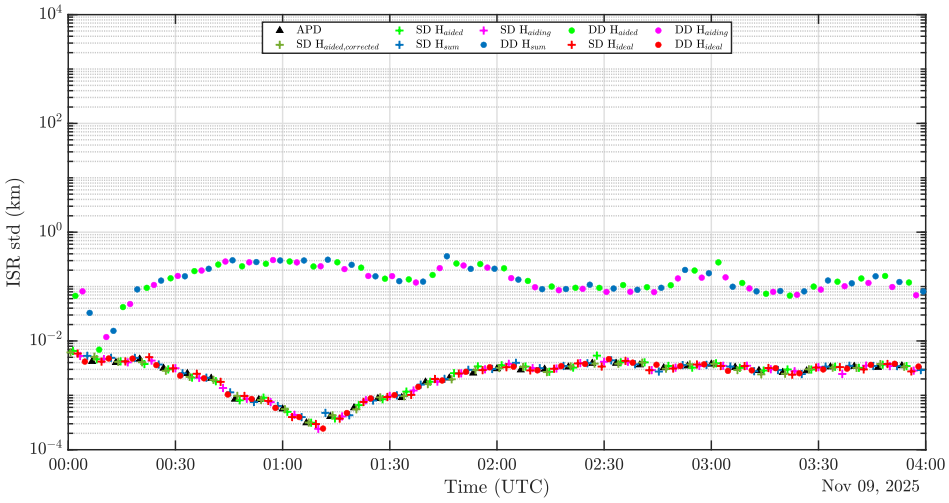

(**b**) ISR std over time.

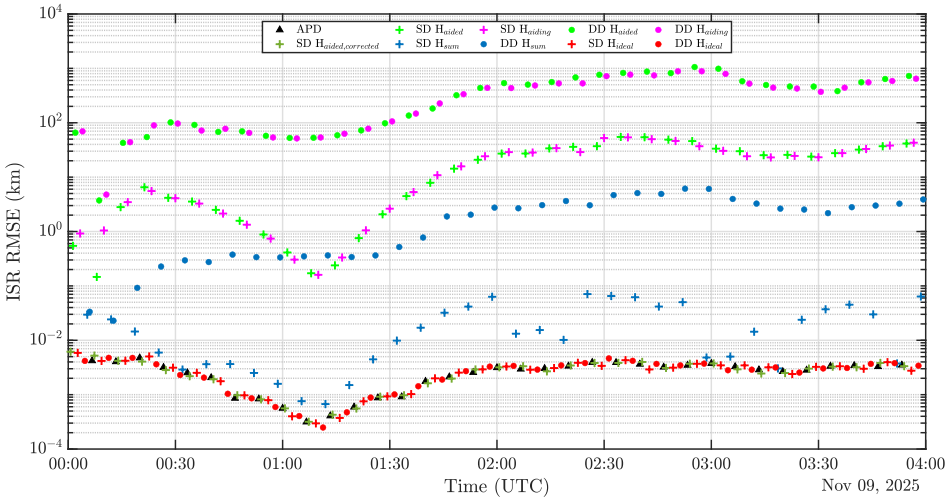

(**c**) ISR RMSE over time.

Figure 10. ISR estimation over time.

The second subfigure of Figure 10 presents the standard deviation of the ISR estimators, as defined by the KPI presented in Equation (25). It can be observed that the presented techniques are split into two groups based on their estimates' variance. Roughly speaking, the DD techniques present a higher variance when compared to the SD techniques, with the exception of DD H_{ideal} which has a variance similar to the SD ranging techniques. The fact that DD techniques overall present a higher variance is expected as applying the SD twice is supposed to decrease the correlated errors but increase the uncorrelated ones, represented by the term Σ_{ij} in Equation (11).

Finally, Figure 10c, which combines both mean and standard deviation in one metric, shows that the estimators SD H_{ideal}, DD H_{ideal}, APD and SD $H_{aided,corrected}$ are the best estimators in absolute in this configuration.

4.1.1. Characterization of the ISV Estimates

The statistics of the ISR were presented above since the final result of interest of the presented techniques consists in the range information. However, as explained in Section 2 and expressed in Equation (1), this range estimation is actually achieved by taking the Euclidean norm of the estimated ISV from the presented algorithms in Section 2. Hence, looking at the statistics of the range, although representative of what happens in a real scenario, they may not highlight the statistical behavior of the presented differential estimators. Therefore, for a better understanding and interpretation of the statistics, Figure 11 shows the statistics of the three components of the ISV estimates independently, based on the terrestrial SD H_{aided} technique as well as the SD H_{ideal} one, in the reference frame Moon-Mean Earth as defined in STK [77]. Figure 11a shows this time even better the clear dependency of the bias introduced by the parallelism assumption and the theta angles depicted in Figure 8. A second observation to be drawn from this alternate error representation is the relationship between the standard deviation of the estimation process and DOP depicted in Figure 6, as per the plateau present a bit later than 0:30 a.m. and the peak present right after 03:00 a.m., due to a combined large DOP and a low visibility. A last thing to be pointed out on graphic Figure 11a is the lower variance in the x-direction, actually corresponding to the direction closest to the Moon-Earth direction, given the spatial distribution of the GNSS satellites as seen by a user at lunar altitudes. When moving to the SD H_{ideal} technique, although the standard deviation remains similar to the terrestrial algorithm estimates, it is noteworthy that the bias of the estimates is reduced to 0 (some noise remains visible due to the practical impossibility of running an infinite number of Monte Carlo simulations).

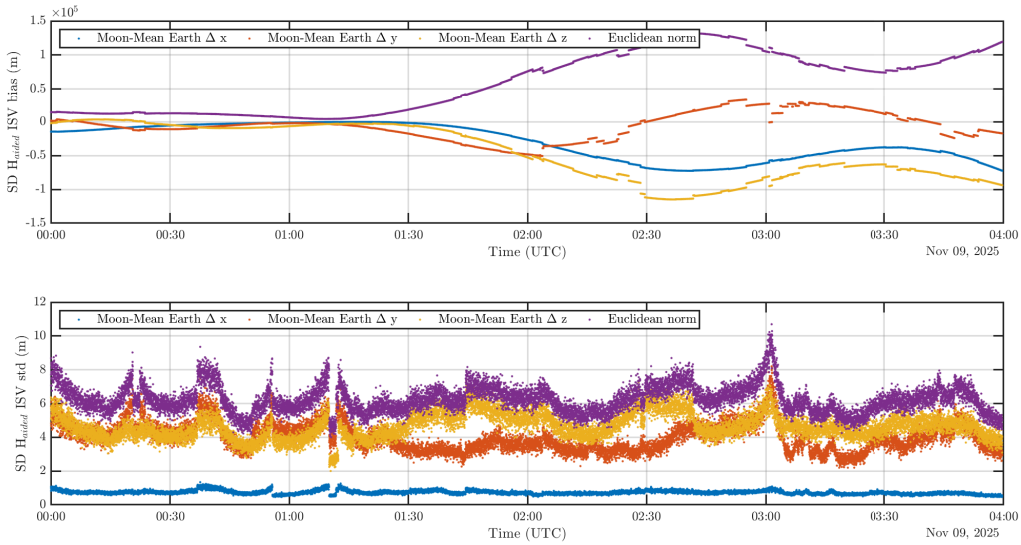

Figure 11. *Cont.*

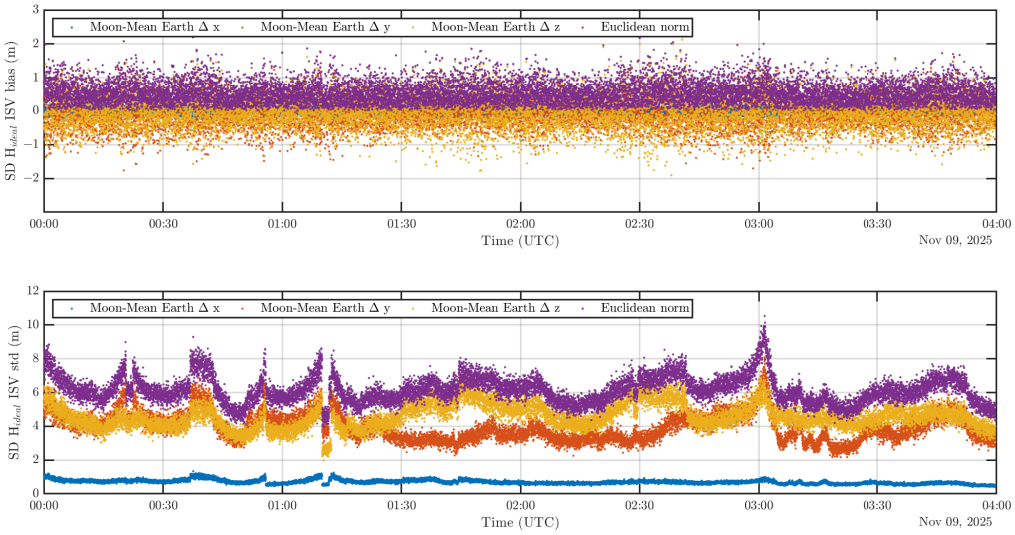

Figure 11. ISV estimation over time.

4.1.2. Impact of Large Orbital Errors

The results presented so far were simulated without satellite orbital errors in order to isolate the impact of the large-scale lunar DGNSS scenario on the performances of the ranging algorithm itself. However, it is important to analyze in such an environment if differential techniques keep their potential to cancel errors correlated among the involved users and, in particular, large satellite orbital errors in case the lunar GNSS receiver must use GNSS ephemerides from the past, as explained in Section 2.2.1. As mentioned in Section 2.2.2, the closer the parallelism assumption is to reality, the better will be the capacity of the ISR estimator to cancel orbital errors. Therefore, Figure 12 shows what would be the residual orbital error on each GNSS SD measurement in the presence of representative satellite orbital errors of 400 m norm as described in Section 2.2.1. This canceling potential is expressed analytically in Equation (23). The residuals individually depend on the original direction of the GNSS satellites orbital errors which was modeled as random in the present simulations. Hence, they vary significantly over the constellation. However, the overall behavior does present a non-negligible correlation with the respective angles depicted in Figure 8. In such a scenario, Figure 12 shows that the residuals of the orbital errors on the SD pseudorange measurements would be upper bounded by a value of 11 m. Despite the very large baseline characteristic of space GNSS ranging scenarios, single differencing the pseudorange measurements hence still has a significant potential to remove systematic errors common to both users.

Figure 13 analyzes through RMSE the impact of large orbital errors on the inter-user ranging performances over time. In comparison with Figure 10c, no apparent effect is present for the terrestrial techniques, most probably due to the domination by the large bias already present. However, what stands out from this new result is the degradation of the APD technique after 02:00 a.m., or when the theta angles become larger overall. APD is overtaken by the differential algorithms, demonstrating the advantage of applying differential techniques at the measurement level to calculate the range information, instead of retrieving it at position-level like it is achieved in APD.

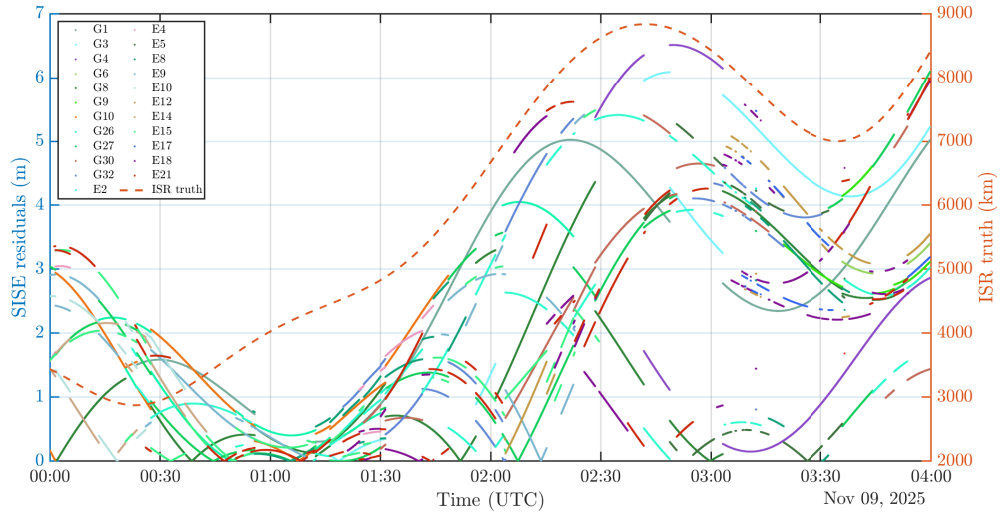

Figure 12. Orbital error residuals on SD measurements.

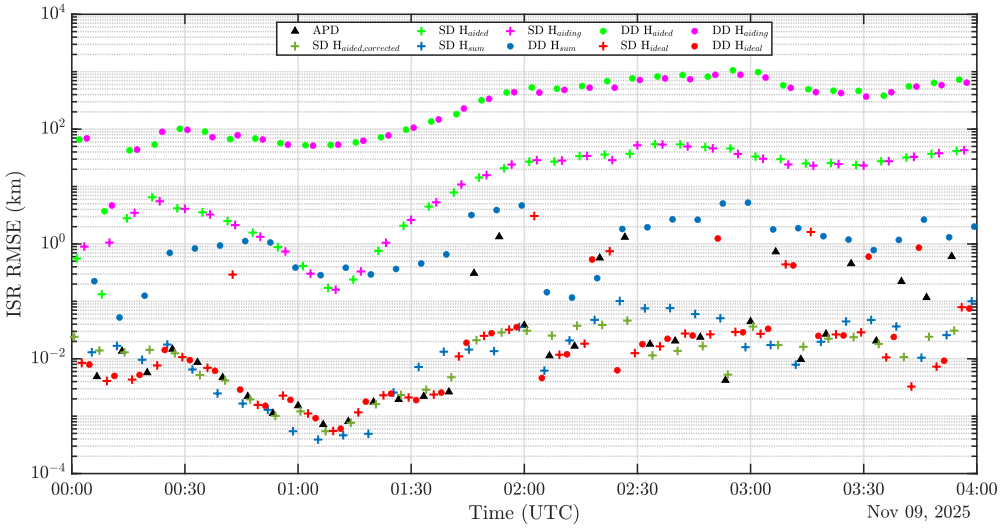

Figure 13. ISR RMSE over time with worst-case SISE.

4.1.3. Impact of Extrapolating the Aiding User's Observables to the Aided User's Timestamp in the Presence of Receiver Clock Biases

Finally, Figure 14 compares the results of the ISR estimation with and without differential clock bias between both users, using a comparison based on the simulated and the experimental results. It shows that such a differential clock bias dramatically impacts the differential techniques. As explained in Section 2.2.1, the large Doppler shifts characteristic of a lunar GNSS scenario makes the ranging algorithms much more sensitive to an error in time correction. Indeed, each receiver needs to estimate its own local clock bias in order to find its own timestamp in the system time frame, and successively, to be able to combine its local measurements with the aiding user. Since a time estimation error will be present for both users, the time offset between their respective set of GNSS measurements that is estimated to extrapolate the aiding measurements at the aided user's timestamps will be affected by errors as well. The large Doppler shifts might magnify these time estimation errors. Therefore, the ranging performances are degraded.

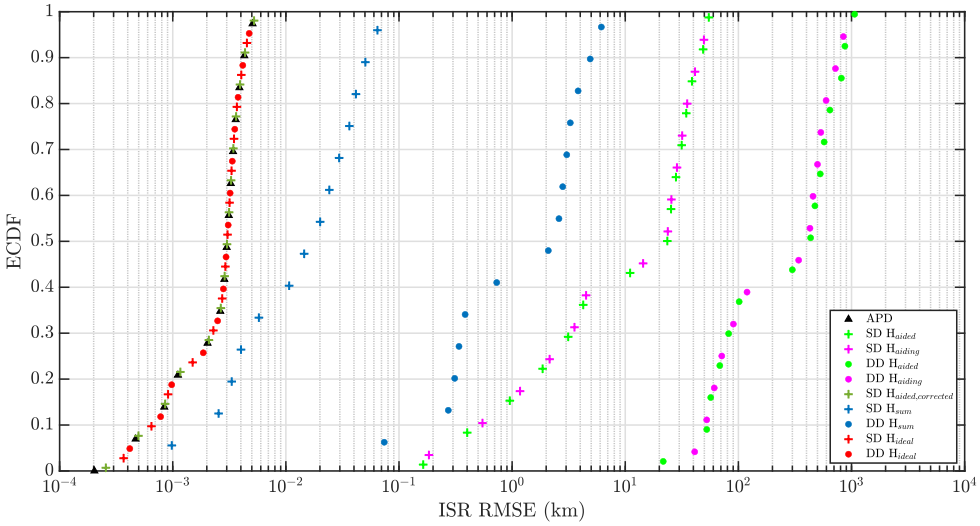

(**a**) eCDF of the RMSE from Monte Carlo simulations (without differential clock bias)

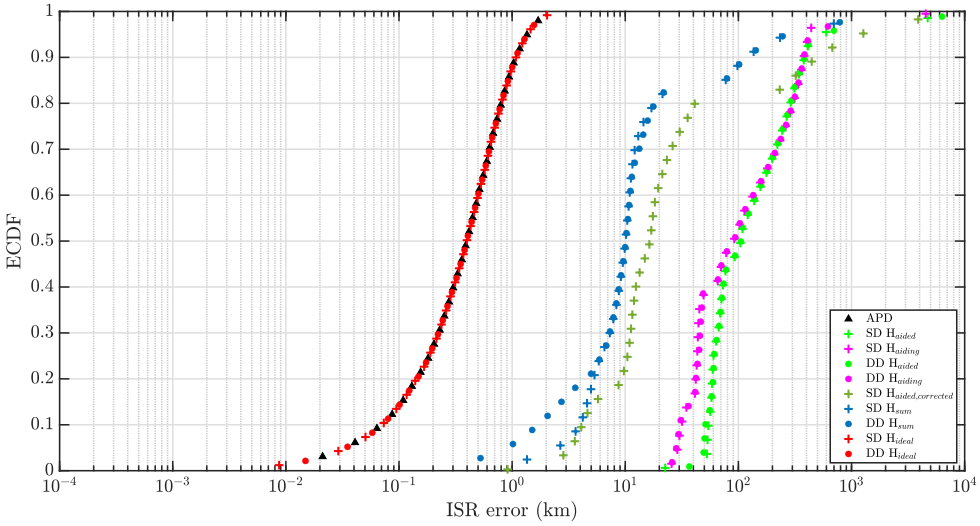

(**b**) eCDF of the RMSE with NaviMoon differential clock bias.

Figure 14. ISR estimation from simulations vs from NaviMoon.

5. Conclusions

This contribution investigated a case of code-based differential GNSS for two lunar orbiters as it has never been conducted before. In particular, it assessed the potential of ISR estimation both through theoretical simulations and HWiL tests using the soon-to-be-flying NaviMoon Galileo-GPS receiver. Doing so, it has shown that commonly used terrestrial algorithms for kinematic code-based differential GNSS ranging techniques are not applicable for a scenario of GNSS receivers in lunar orbits, despite their individual ability to navigate using GNSS signals from terrestrial constellations. Indeed, when using the standard code-based DGNSS algorithm, a significant bias is introduced, whose magnitude increases with the angular separation between the two users with respect to the GNSS constellation. This geometrical bias is introduced by the parallelism assumption between steering vectors from the two users involved to each visible GNSS satellite, which has been taken for granted in ground applications. This contribution hence analyzed the potential to improve the DGNSS ranging algorithm in space with respect to the violation of the parallelism assumption while keeping the algorithm low complexity and linear for lunar scenarios. It showed that potential updates of the steering vectors in the design matrix of the SD and DD LS estimation solutions can significantly reduce or even cancel this bias. In particular, a technique called “ideal” in the present contribution and found in

the literature in the context of Doppler-based LEO positioning based on SoP, has proven to show added value. It is based on defining a specific steering vector at each epoch for which the projection of the baseline on this given direction exactly equals the difference in geometrical ranges to the GNSS satellite. Hence, this technique reduces the bias that the terrestrial assumption was introducing in this linear estimator to zero. The variance of the presented estimators is consistent with the DOP calculated based on the GNSS satellites commonly visible to both users at the same time. This paper further analyzed the presented algorithms by assessing their potential to cancel errors correlated between the involved users despite the large-scale geometry of such an environment. In the presence of a worst-case scenario of 400 m of GNSS orbital errors, the presented differential algorithms proved to overtake the APD technique in case of a large baseline. Another point this work looked into is the sensitivity of the algorithms to the quality of the receiver's clock bias estimation. This is particularly important for a scenario of orbiters given the high relative velocities and the large ISR variation rate over the timestamp offset between the set of GNSS measurements of the two users. Given the large Doppler shifts characteristic of this kind of GNSS scenarios, an error in the receiver's clock bias estimation can significantly decrease the ranging performances.

Author Contributions: Conceptualization, A.D., A.M. and F.D.; methodology, A.D. and A.M.; software, A.D.; validation, A.D., A.M. and F.D.; formal analysis, A.D.; investigation, A.D.; resources, A.M. and F.D.; data curation, A.D.; writing—original draft preparation, A.D.; writing—review and editing, A.D., A.M. and F.D.; visualization, A.D.; supervision, A.M. and F.D.; project administration, F.D.; funding acquisition, A.M. and F.D. All authors have read and agreed to the published version of the manuscript.

Funding: This research was co-funded by European Space Agency Contract No. 4000134565/21/NL/GLC/my. A. Minetto acknowledges funding from the research contract no. 32-G-13427-5 DM 1062/2021 funded within the Programma Operativo Nazionale (PON) Ricerca ed Innovazione of the Italian Ministry of University and Research (MUR). The content of the present article reflects solely the authors' view and by no means represents the official view of the European Space Agency (ESA). In any reproduction of this article, there should not be any suggestion that ESA or this article endorses any specific organization or product. The use of the ESA logo is not permitted. This notice should be preserved along with the article's original URL.

Data Availability Statement: The data presented in this study are available on request from the corresponding author, the data are not publicly available due to ESA confidentiality policies.

Conflicts of Interest: The authors declare no conflict of interest.

Abbreviations

The following abbreviations are used in this manuscript:

APD	Absolute Positions Differencing
ASI	Italian Space Agency
CP	Cooperative Positioning
DD	Double Differences
DOP	Dilution of Precision
DGNSS	Differential GNSS
eCDF	empirical Cumulative Distribution Function
ECEF	Earth Centered Earth Fixed
ELFO	Elliptical Lunar Frozen Orbit
ESA	European Space Agency
GNSS	Global Navigation Satellite System
GPS	Global Positioning System
GRACE	Gravity Recovery And Climate Experiment
HPOP	High-Precision Orbit Propagator
HWiL	Hardware-in-the-Loop
ISR	Inter-Spacecraft Range

LAMBDA	Least Square Ambiguity Decorrelation Adjustment
LEO	Low-Earth Orbit
LLFO	Low Lunar Frozen Orbit
LoS	Line-of-Sight
LPF	Lunar Pathfinder
LS	Least Squares
NASA	National Aeronautics and Space Administration
PNT	Positioning, Navigation and Timing
PVT	Position Velocity Time
RF	Radio Frequency
RFCS	Radio Frequency Constellation Simulator
RINEX	Receiver Independent Exchange Format
RMSE	Root Mean Square Error
RTK	Real Time Kinematic
RTT	Round-trip Time
SD	Single Differences
SISE	Signal In Space Error
SoP	Signal of Opportunity
SSV	Space Service Volume
STK	Systems Tool Kit
SPP	Single Point Position
SSTL	Surrey Satellite Technology Ltd
TM/TC	Telemetry and Telecommand
ToF	Time of Flight
TRL	Technology Readiness Level
UTC	Coordinated Universal Time
VMMO	Volatile and Mineralogy Mapping Orbiter

References

1. European Space Agency. Moonlight: Connecting Earth with the Moon. 2021. Available online: https://www.esa.int/ESA_Multimedia/Videos/2020/11/Moonlight_connecting_Earth_with_the_Moon (accessed on 31 May 2024).
2. Flahaut, J.; Carpenter, J.; Williams, J.P.; Anand, M.; Crawford, I.; Van Westrenen, W.; Füri, E.; Xiao, L.; Zhao, S. Regions of interest (ROI) for future exploration missions to the lunar South Pole. *Planet. Space Sci.* **2020**, *180*, 104750. [CrossRef]
3. Mazarico, E.; Barker, M.K.; Jagge, A.M.; Britton, A.W.; Lawrene exploration missions to the lunar South Pole. *Planet. Space Sci.* **2020**, *180*, 104750.
4. Armenta, J.M.R.; Bazmohammadi, N.; Saha, D.; Vasquez, J.C.; Guerrero, J.M. Optimal multi-site selection for a PV-based lunar settlement based on a novel method to estimate sun illumination profiles. *Adv. Space Res.* **2023**, *71*, 2059–2074. [CrossRef]
5. Leone, G.; Ahrens, C.; Korteniemi, J.; Gasparri, D.; Kereszturi, A.; Martynov, A.; Schmidt, G.W.; Calabrese, G.; Joutsenvaara, J. Sverdrup-Henson crater: A candidate location for the first lunar South Pole settlement. *Iscience* **2023**, *26*, 107853. [CrossRef] [PubMed]
6. Satellite Technology Ltd. Lunar Pathfinder. 2023. Available online: https://www.sstl.co.uk/getmedia/edaaa697-405c-458d-8394-97f83130d54a/Lunar-Pathfinder-Service-Guide-V2-2.pdf&ved=2ahUKEwjgtYKH1MuHAxXH4zQHHdkxBqEQFnoECBkQAQ&usg=AOvVaw3BioQ_48cGYlK5YuC3bpFE (accessed on 31 May 2024).
7. Parker, J.J.; Dovis, F.; Anderson, B.; Ansalone, L.; Ashman, B.; Bauer, F.H.; D'Amore, G.; Facchinetti, C.; Fantinato, S.; Impresario, G.; et al. The lunar GNSS receiver experiment (lugre). In Proceedings of the 2022 International Technical Meeting of The Institute of Navigation, Long Beach, CA, USA, 25–27 January 2022; pp. 420–437.
8. United Nations Office for Outer Space Affairs. *The Interoperable Global Navigation Satellite Systems Space Service Volume*; United Nations: Vienna, Austria, 2021.
9. Lunar Resources Registry. List of Planned Missions to the Moon. 2024. Available online: https://lunarresourcesregistry.com/list-of-planned-mission-to-the-moon/ (accessed on 31 May 2024).
10. European Space Agency. Telling Time on the Moon. 2023. Available online: https://www.esa.int/Applications/Satellite_navigation/Telling_time_on_the_Moon (accessed on 31 May 2024).
11. Selva, D.; Golkar, A.; Korobova, O.; Cruz, I.L.i.; Collopy, P.; de Weck, O.L. Distributed earth satellite systems: What is needed to move forward? *J. Aerosp. Inf. Syst.* **2017**, *14*, 412–438. [CrossRef]
12. Minetto, A.; Gurrieri, A.; Dovis, F. A cognitive particle filter for collaborative DGNSS positioning. *IEEE Access* **2020**, *8*, 194765–194779. [CrossRef]
13. Weng, D.; Gan, X.; Chen, W.; Ji, S.; Lu, Y. A new DGNSS positioning infrastructure for android smartphones. *Sensors* **2020**, *20*, 487. [CrossRef] [PubMed]
14. Kaplan, E.D.; Hegarty, C. *Understanding GPS/GNSS: Principles and Applications*; Artech House: Norwood, MA, USA, 2017.

15. Odolinski, R.; Teunissen, P.J. Low-cost, high-precision, single-frequency GPS–BDS RTK positioning. *GPS Solut.* **2017**, *21*, 1315–1330. [CrossRef]
16. Choi, B.K.; Yoon, H.S.; Lee, S.J. Performance analysis of long baseline relative positioning using dual-frequency GPS/BDS measurements. *J. Position. Navig. Timing* **2019**, *8*, 87–94.
17. Mohino, E.; Gende, M.; Brunini, C. Improving long baseline (100–300 km) differential GPS positioning applying ionospheric corrections derived from multiple reference stations. *J. Surv. Eng.* **2007**, *133*, 1–5. [CrossRef]
18. Cheng, J.; Jiang, C.; Li, L.; Jia, C.; Qi, B.; Li, J. Long baseline tightly coupled DGNSS positioning with ionosphere-free inter-system bias calibration. *Remote Sens.* **2020**, *13*, 67. [CrossRef]
19. Kubo, Y.; Tanaka, H.; Ohashi, M.; Sugimoto, S. Long baseline GNSS relative positioning with estimating ionospheric and tropospheric delays and their gradients. In Proceedings of the ISCIE International Symposium on Stochastic Systems Theory and Its Applications, Shiga, Japan, 28–29 October 2011; Volume 2011, pp. 228–235.
20. Liu, K.; Lim, H.B.; Frazzoli, E.; Ji, H.; Lee, V.C.S. Improving Positioning Accuracy Using GPS Pseudorange Measurements for Cooperative Vehicular Localization. *IEEE Trans. Veh. Technol.* **2014**, *63*, 2544–2556. [CrossRef]
21. Minetto, A.; Dovis, F. On the Information Carried by Correlated Collaborative Ranging Measurements for Hybrid Positioning. *IEEE Trans. Veh. Technol.* **2020**, *69*, 1419–1427. [CrossRef]
22. Minetto, A.; Bello, M.C.; Dovis, F. DGNSS cooperative positioning in mobile smart devices: A proof of concept. *IEEE Trans. Veh. Technol.* **2022**, *71*, 3480–3494. [CrossRef]
23. Tahir, M.; Afzal, S.S.; Chughtai, M.S.; Ali, K. On the Accuracy of Inter-Vehicular Range Measurements Using GNSS Observables in a Cooperative Framework. *IEEE Trans. Intell. Transp. Syst.* **2018**, *20*, 682–691. [CrossRef]
24. D'Amico, S.; Carpenter, J.R. Satellite formation flying and rendezvous. *Position Navig. Timing Technol. 21st Century Integr. Satell. Navig. Sens. Syst. Civ. Appl.* **2020**, *2*, 1921–1946.
25. D'Amico, S.; Montenbruck, O. Differential GPS: An enabling technology for formation flying satellites. In *Small Satellite Missions for Earth Observation: New Developments and Trends*; Springer: Berlin/Heidelberg, Germany, 2010; pp. 457–465.
26. Chen, P.; Shu, L.; Ding, R.; Han, C. Kinematic Single-Frequency Relative Positioning for LEO Formation Flying Mission. *GPS Solut.* **2015**, *19*, 525–535. [CrossRef]
27. Allende-Alba, G.; Montenbruck, O. Robust and precise baseline determination of distributed spacecraft in LEO. *Adv. Space Res.* **2016**, *57*, 46–63. [CrossRef]
28. Montenbruck, O.; D'Amico, S. GPS based relative navigation. In *Distributed Space Missions for Earth System Monitoring*; Springer: Berlin/Heidelberg, Germany, 2012; pp. 185–223.
29. Mahfouz, A.; Menzio, D.; Dalla Vedova, F.; Voos, H. GNSS-based baseline vector determination for widely separated cooperative satellites using L1-only receivers. *Adv. Space Res.* **2024**, *73*, 5570–5581. [CrossRef]
30. Tancredi, U.; Renga, A.; Grassi, M. Ionospheric path delay models for spaceborne GPS receivers flying in formation with large baselines. *Adv. Space Res.* **2011**, *48*, 507–520. [CrossRef]
31. Allende-Alba, G.; Montenbruck, O.; Jäggi, A.; Arnold, D.; Zangerl, F. Reduced-dynamic and kinematic baseline determination for the Swarm mission. *GPS Solut.* **2017**, *21*, 1275–1284. [CrossRef]
32. Renga, A.; Grassi, M.; Tancredi, U. Relative navigation in LEO by carrier-phase differential GPS with intersatellite ranging augmentation. *Int. J. Aerosp. Eng.* **2013**, *2013*, 627509. [CrossRef]
33. Kawano, I.; Mokuno, M.; Kasai, T.; Suzuki, T. First autonomous rendezvous using relative GPS navigation by ETS-VII. *Navigation* **2001**, *48*, 49–56. [CrossRef]
34. Kroes, R.; Montenbruck, O.; Bertiger, W.; Visser, P. Precise GRACE baseline determination using GPS. *GPS Solut.* **2005**, *9*, 21–31. [CrossRef]
35. Kahr, E.; Roth, N.; Montenbruck, O.; Risi, B.; Zee, R.E. GPS relative navigation for the CanX-4 and CanX-5 formation-flying nanosatellites. *J. Spacecr. Rocket.* **2018**, *55*, 1545–1558. [CrossRef]
36. Capuano, V.; Harvard, A.; Chung, S.J. On-board cooperative spacecraft relative navigation fusing GNSS with vision. *Prog. Aerosp. Sci.* **2022**, *128*, 100761. [CrossRef]
37. Guffanti, T.; Bell, T.; Low, S.Y.; Murray-Cooper, M.; D'Amico, S. Autonomous Guidance Navigation and Control of the VISORS Formation-Flying Mission. *arXiv* **2023**, arXiv:2309.16698.
38. Low, S.Y.; D'Amico, S. Precise Distributed Satellite Navigation: Differential GPS with Sensor-Coupling for Integer Ambiguity Resolution. In Proceedings of the 2024 IEEE Aerospace Conference, Big Sky, MT, USA, 2–9 March 2024; pp. 1–18.
39. Minetto, A.; Ammirante, G.; Stesina, F.; Dovis, F.; Corpino, S. DGNSS Ranging for CubeSat Rendezvous and Docking Manoeuvres at LEO. In Proceedings of the 2023 IEEE 10th International Workshop on Metrology for AeroSpace (MetroAeroSpace), Milan, Italy, 19–21 June 2023; pp. 597–602.
40. Cai, Y.; Li, Y.; Wang, Z. Real-time High-precision Baseline Measurement of Satellite Formation Flying Based on GNSS. *Adv. Space Res.* **2024**, *73*, 5171–5187. [CrossRef]
41. Delépaut, A.; Schönfeldt, M.; Giordano, P.; Blonski, D.; Sarnadas, R.; Ries, L.; Ventura-Traveset, J. A System Study for Cislunar Radio Navigation Leveraging the Use of Realistic Galileo and GPS Signals. In Proceedings of the 32nd International Technical Meeting of the Satellite Division of The Institute of Navigation (ION GNSS+ 2019), Miami, FL, USA, 16–19 September 2019; pp. 1199–1219.

42. Delépaut, A.; Giordano, P.; Ventura-Traveset, J.; Blonski, D.; Schönfeldt, M.; Schoonejans, P.; Aziz, S.; Walker, R. Use of GNSS for lunar missions and plans for lunar in-orbit development. *Adv. Space Res.* **2020**, *66*, 2739–2756. [CrossRef]
43. Schonfeldt, M.; Grenier, A.; Delépaut, A.; Giordano, P.; Swinden, R.; Ventura-Traveset, J.; Blonski, D.; Hahn, J. A System Study about a Lunar Navigation Satellite Transmitter System. In Proceedings of the 2020 European Navigation Conference (ENC), Dresden, Germany, 23–24 November 2020; pp. 1–10. [CrossRef]
44. Yang, W.; Liu, Y.; Liu, F. An improved relative GNSS tracking method utilizing single frequency receivers. *Sensors* **2020**, *20*, 4073. [CrossRef]
45. Kelbel, D.; Lee, T.; Long, A.; Carpenter, J.R.; Gramling, C. Evaluation of relative navigation algorithms for formation-flying satellites. In Proceedings of the 2001 Flight Mechanics Symposium, Greenbelt, MD, USA, 19–21 June 2001.
46. Giordano, P.; Malman, F.; Swinden, R.; Zoccarato, P.; Ventura-Traveset, J. The Lunar Pathfinder PNT Experiment and Moonlight Navigation Service: The Future of Lunar Position, Navigation and Timing. In Proceedings of the 2022 International Technical Meeting of The Institute of Navigation, Long Beach, CA, USA, 25–27 January 2022; pp. 632–642.
47. Gogoi, N.; Minetto, A.; Dovis, F. On the Cooperative Ranging between Android Smartphones Sharing Raw GNSS Measurements. In Proceedings of the 2019 IEEE 90th Vehicular Technology Conference (VTC2019-Fall), Honolulu, HI, USA, 22–25 September 2019; pp. 1–5. [CrossRef]
48. Hofmann-Wellenhof, B.; H. Lichtenegger, J.C. *Global Positioning System: Theory and Practice*; Springer Science & Business Media: Berlin/Heidelberg, Germany, 2012.
49. Teunissen, P.J.; Montenbruck, O. *Springer Handbook of Global Navigation Satellite Systems*; Springer: Berlin/Heidelberg, Germany, 2017; Volume 10.
50. Subirana, J.S.; Zornoza, J.; Hernández-Pajares, M. *GNSS Data Processing*; Vol. I: Fundamentals and Algorithms, ESA Communications; European Space Agency: Noordwijk, The Netherlands, 2013.
51. de Ponte Müller, F.; Steingass, A.; Strang, T. Zero-baseline measurements for relative positioning in vehicular environments. In Proceedings of the 6th European Workshop on GNSS Signals and Signal Processing of Universität der Bundeswehr, Munchen, Germany, 5–6 December 2013.
52. Ong, R.; Lachapelle, G. Use of GNSS for vehicle-pedestrian and vehicle-cyclist crash avoidance. *Int. J. Veh. Saf.* **2011**, *5*, 137–155. [CrossRef]
53. Alam, N.; Balaei, A.T.; Dempster, A.G. Positioning enhancement with double differencing and DSRC. In Proceedings of the 23rd International Technical Meeting of The Satellite Division of the Institute of Navigation (ION GNSS 2010), Portland, OR, USA, 21–24 September 2010; pp. 1210–1218.
54. Yang, D.; Zhao, F.; Liu, K.; Lim, H.B.; Frazzoli, E.; Rus, D. A GPS pseudorange based cooperative vehicular distance measurement technique. In Proceedings of the 2012 IEEE 75th Vehicular Technology Conference (VTC Spring), Yokohama, Japan, 6–9 May 2012; pp. 1–5.
55. Hedgecock, W.; Maroti, M.; Sallai, J.; Volgyesi, P.; Ledeczi, A. High-accuracy differential tracking of low-cost GPS receivers. In Proceedings of the 11th Annual International Conference on Mobile Systems, Applications, and Services, Taipei, Taiwan, 25–28 June 2013; pp. 221–234.
56. Lin, K.; Zhan, X.; Huang, J. GNSS signals ionospheric propagation characteristics in space service volume. *Int. J. Space Sci. Eng.* **2019**, *5*, 223–241. [CrossRef]
57. Galluzzo, G.; Binda, S.; Blonksi, D.; Gonzalez, F.; Spinelli, E.; Swinden, R.; Rodriguez, R.L.; Falcone, M. Measuring Galileo Performance: Navigation and Timing Performance Figures of Merit | Part 2. *InsideGNSS* **2018**. Available online: https://insidegnss.com/measuring-galileo-performance-navigation-and-timing-performance-figures-of-merit-part-2/ (accessed on 31 May 2024).
58. DOD. *Global Positioning System Standard Positioning Service Performance Standard*, 5th ed.; 2020. Available online: https://www.gps.gov/technical/ps/2020-SPS-performance-standard.pdf (accessed on 31 May 2024).
59. uBlox. *GPS Essentials of Satellite Navigation*; uBlox: Thalwil, Switzerland, 2007.
60. Tancredi, U.; Renga, A.; Grassi, M. Real-time relative positioning of spacecraft over long baselines. *J. Guid. Control Dyn.* **2014**, *37*, 47–58. [CrossRef]
61. Wu, N.; Qin, H.; Zhao, C. Long-baseline Differential Doppler Positioning Using Space-based SOP Based on BPVGMM. *IEEE Trans. Instrum. Meas.* **2023**, *72*, 8503610. [CrossRef]
62. AGI. STK: High-Precision Orbit Propagator (HPOP). 2018. Available online: https://help.agi.com/stk/11.4.1/index.htm#hpop/hpop.htm (accessed on 31 May 2024).
63. Konopliv, A.S.; Park, R.S.; Yuan, D.N.; Asmar, S.W.; Watkins, M.M.; Williams, J.G.; Fahnestock, E.; Kruizinga, G.; Paik, M.; Strekalov, D.; et al. The JPL lunar gravity field to spherical harmonic degree 660 from the GRAIL Primary Mission. *J. Geophys. Res. Planets* **2013**, *118*, 1415–1434. [CrossRef]
64. Rowe, S.; Kruzelecky, R.; Murzionak, P.; Sinclair, I.; Corriveau, M.; Walker, R.; Vennekens, J.; Gao, Y.; Bridges, C.; Baresi, N.; et al. Lunar volatile and mineralogy mapping orbiter (VMMO): Viable science from lunar CubeSats. In Proceedings of the 35th Annual Small Satellite Conference of Utah State University Logan, Logan, UT, USA, 7–12 August 2021.
65. Surrey Satellite Technology Ltd. Lunar Pathfinder Data Relay Satellite in Orbit around the Moon. 2020. Available online: https://www.sstl.co.uk/getmedia/690f1da3-a935-4c4d-b48c-616ac8417cb1/LunarPathfinder-UserManual-WebSite-v003.pdf (accessed on 31 May 2024).

66. Surrey Satellite Technology Ltd. Lunar Pathfinder. 2024. Available online: https://www.sstl.co.uk/space-portfolio/missions-in-build/2024/lunar-pathfinder (accessed on 31 May 2024).
67. Nanosats Database. VMMO (Volatile and Mineralogy Mapping Orbiter). 2023. Available online: https://www.nanosats.eu/sat/vmmo (accessed on 31 May 2024).
68. Bramanto, B.; Gumilar, I.; Taufik, M.; Hermawan, I.M.D. Long-range single baseline RTK GNSS positioning for land cadastral survey mapping. In Proceedings of the E3S Web of Conferences, Dnipro, Ukraine, 25–27 June 2019; EDP Sciences: Les Ulis, France, 2019; Volume 94, p. 01022.
69. Gumilar, I.; Bramanto, B.; Rahman, F.F.; Hermawan, I.M.D. Variability and performance of short to long-range single baseline RTK GNSS positioning in Indonesia. In Proceedings of the E3S Web of Conferences, Dnipro, Ukraine, 25–27 June 2019; EDP Sciences: Les Ulis, France, 2019; Volume 94, p. 01012.
70. Giralo, V.; D'Amico, S. Precise real-time relative orbit determination for large-baseline formations using GNSS. In Proceedings of the 2021 International Technical Meeting of The Institute of Navigation, Online, 25–28 January 2021; pp. 366–384.
71. SpacePNT. SpacePNT: NaviMoon. 2023. Available online: https://spacepnt.com/navimoon/ (accessed on 31 May 2024).
72. Navigation Center United States Coast Guard, U.S. Department of Homeland Security. GPS Technical References. 2024. Available online: https://navcen.uscg.gov/gps-technical-references (accessed on 31 May 2024).
73. Betz, J.W.; Fine, P.B. Effect of narrow correlator spacing on code tracking accuracy. In Proceedings of the 2000 National Technical Meeting of the Institute of Navigation, Anaheim, CA, USA, 26–28 January 2000; pp. 716–723.
74. Surrey Satellite Technology Ltd. Satnav from Earth to the Moon. 2023. Available online: https://www.esa.int/ESA_Multimedia/Images/2023/06/Satnav_from_Earth_to_the_Moon (accessed on 31 May 2024).
75. NAVISP. How to Navigate on the Moon? 2023. Available online: https://navisp.esa.int/news/article/How%20to%20navigate%20on%20the%20moon%3F (accessed on 31 May 2024).
76. European Space Agency Earth-Moon Navigation/System Study and Development of Highly-Sensitive Spaceborne Receiver Prototype (NAVISP-EL1-023). 2023. Available online: https://navisp.esa.int/uploads/files/documents/Navisp%20EL1-023%20FInal%20Presentation_static.pdf (accessed on 31 May 2024).
77. AGI. Descriptions of Coordinate Systems in STK. 2018. Available online: https://help.agi.com/stk/11.4.1/index.htm#stk/referenceFramesCBdescriptions.htm#Inertial (accessed on 31 May 2024).

Disclaimer/Publisher's Note: The statements, opinions and data contained in all publications are solely those of the individual author(s) and contributor(s) and not of MDPI and/or the editor(s). MDPI and/or the editor(s) disclaim responsibility for any injury to people or property resulting from any ideas, methods, instructions or products referred to in the content.